

# Angle-Tuned Gross-Neveu Quantum Criticality in Twisted Bilayer Graphene: A Quantum Monte Carlo Study

Cheng Huang,<sup>1</sup> Nikolaos Parthenios,<sup>2,3</sup> Maksim Ulybyshev,<sup>4</sup> Xu  
Zhang,<sup>1,5</sup> Fakher F. Assaad,<sup>4,6</sup> Laura Classen,<sup>2,3,\*</sup> and Zi Yang Meng<sup>1,†</sup>

<sup>1</sup>*Department of Physics and HK Institute of Quantum Science & Technology,  
The University of Hong Kong, Pokfulam Road, Hong Kong*

<sup>2</sup>*Max Planck Institute for Solid State Research, Heisenbergstr. 1, 70569 Stuttgart Germany*

<sup>3</sup>*School of Natural Sciences, Technische Universität München, 85748 Garching, Germany*

<sup>4</sup>*Institut für Theoretische Physik und Astrophysik, Universität Würzburg, 97074 Würzburg, Germany*

<sup>5</sup>*Department of Physics and Astronomy, Ghent University, Krijgslaan 281, 9000 Gent, Belgium*

<sup>6</sup>*Würzburg-Dresden Cluster of Excellence ct.qmat, Am Hubland, 97074 Würzburg, Germany*

(Dated: December 17, 2024)

The tunability of twisted bilayer graphene (TBG) in particular and the 2D moiré materials in general has revealed fascinating quantum many-body states of matter, such as correlated insulators [1] and superconductivity [2]. Unstrained magic-angle TBG at the charge-neutrality point is understood, both experimentally [1, 3] and theoretically [4–6], as a correlated insulating state due to the interplay of long-range Coulomb interaction and the quantum metric of the flat bands. However, the fate of the state as one continuously tunes the twist angle is still largely unknown. Experimentally with the new development of the quantum twisting microscope [7] such continuous tuning of the twist angle has become possible. Theoretically, it was suggested that due to the effective change of interaction strength, angle-tuned TBG might exhibit the first realization of the quantum critical point (QCP) between a correlated insulator and a Dirac semimetal [8] – a condensed matter incarnation of the chiral phase transition of the Gross-Neveu (GN) model studied in the context of quantum chromo dynamics [9, 10]. Here we show that TBG indeed realises an angle-tuned phase transition between a Dirac semimetal and an insulator consistent with a GN quantum criticality in a numerically exact calculation. The transition occurs because the angle effectively tunes the relative weight of kinetic and interaction energy and we map out how this qualitatively changes the single-particle excitation spectrum. Our study is possible due to the recently developed continuous field momentum-space quantum Monte Carlo method, which can fully take into account the long-range Coulomb and quantum metric of flat bands [11]. From the single-particle spectrum, free energy and the analysis of the order parameter of the insulating phase, at system sizes that were not possible before, we find a critical angle of  $\Theta_c \sim 1.20(1)^\circ$ . This offers the exciting possibility that by tuning away from the magic angle ( $1.08^\circ$ ), pristine TBG can mimic a fundamental phase transition of Dirac fermions.

## INTRODUCTION

Twisted bilayer graphene (TBG) has emerged as a tunable platform for studying the behavior of the interplay of correlated electrons and quantum metrics. While its low-energy physics is given by weakly-interacting Dirac electrons for relatively small twisted angles [12–16], narrow bands and strong interactions arise near a magic angle (MA)  $\sim 1.08^\circ$  given by a resonance condition between layer-hybridisation and twist-induced band-energy shifts [17–20]. The bands even become exactly flat and topologically non-trivial at the MA in the chiral, particle-hole symmetric limit which arises for small angles without interlayer tunneling between equal-sublattice sites [21–23]. At the MA, a rich phase diagram as function of filling and temperature was revealed in experiments including correlated insulators, superconductivity, orbital magnetism, and strange metallicity [1–3, 24–27].

Further parameters such as strain, pressure, or magnetic field also play an important role for TBG’s non-trivial phase structure [28–34]. However, the twisted angle as the perhaps most impactful tuning parameter is less explored. While first insights about the angle dependence were obtained from comparison of different experiments or different domains in scanning tunnelling measurements, recent developments made it now

also possible to systematically tune the angle *in-situ*, e.g., via a quantum twisting microscope [7], targeted bending [35], or manipulation of top rotators with an atomic-force-microscopy tip [36] or polymer handles [37]. This raises the question of how the intricate interplay of the strong interaction, band geometry, and topology develops as a function of the twist angle and how angle-tuning can be exploited to optimize and explore phenomena beyond the currently known phase diagram.

Motivated by this, we here investigate the interacting band structure and phases of TBG for a range of twisted angles via unbiased quantum Monte Carlo (QMC) simulations. We perform calculations for the continuum model of TBG at charge neutrality  $\nu = 0$  for realistic parameters [17, 18]. Better than the previously developed momentum-space QMC method for TBG by some of us [11, 38–43], here we employ continuous auxiliary fields and a global update scheme, inspired by the hybrid Monte Carlo method [44], such that the computational complexity is greatly reduced by a factor of the system size and much higher momentum resolution can be accessed (see details in the Method section). With such methodological innovation, we find a continuous phase transition from the gapped correlated insulator phase close to the MA to a Dirac semimetal as a function of the twisted angle. In TBG of unstrained setups, gaps at charge neutrality due to Kramers intervalley

coherence (KIVC) [5, 45, 46] decrease when the twisted angle deviates from MA, and those of  $K_{1,2}$  close continuously at  $\Theta_c = 1.20(1)^\circ$  where Dirac spectra are restored. Such a phase transition spontaneously breaks the chiral symmetry of Dirac fermions and the corresponding quantum critical point (QCP) is consistent with a scenario of relativistic fermionic quantum criticality.

The effective model in this case is given by a Yukawa-Gross-Neveu model [49] with emergent Lorentz invariance [50–53], which interestingly is also used as effective low-energy model in quantum chromodynamics [9]. In recent years consensus on the quantum critical behaviour of GN transitions has emerged on a quantitative level between field-theoretical and numerical methods [54–72]. However, possible experimental realizations remain rare up to now. Organic conductors show precursors of the transition, but a quantum critical point is still elusive [73–75]. While graphene was extensively studied as a potential platform to realize such an interaction-driven transition, the Coulomb interaction in pristine graphene is eventually found to be too weak to realise a correlated insulating state. TBG on the other hand, offers the new opportunity to tune the relative weight of Coulomb interaction and Dirac dispersion by twisting away from the MA. In this way, we indeed observe the GN-QCP from our unbiased QMC simulations of the single-particle spectrum and thermodynamic free energy measurements.

Furthermore, we argue that the angle-tuned quantum phase transition towards the KIVC order in TBG falls into the chiral XY Gross-Neveu (GN) universality classes [10, 76–78]. To demonstrate consistency of the critical behavior with the QMC data, we calculate the characteristic critical exponents based on results from four-loop perturbative calculations [59, 70] for  $N_f = 16$  fermion flavours from spin, valley, mini-valley, and sublattice at  $\nu = 0$  and have obtained consistent results from our simulations on the IVC order parameter of the GN-QCP and the theory prediction.

## RESULTS

### Model and continuous-field Monte Carlo

The kinetic part of our Hamiltonian comes from the continuum model [17, 18]. At MA of  $\Theta = 1.08^\circ$ , there emerges two low-energy flat bands, while the remote bands separates far away around 50 meV, with inter-layer inter-sublattice hopping  $u_1 = 110$  meV and intra-sublattice hopping  $u_0 = 60$  meV [22, 40]. The detailed dispersions of the continuum model are shown in Fig. 6 in the Method section. We note that for the non-interacting continuum model, Dirac cones are always present at the corners of the moiré Brillouin zone (mBZ) with momenta  $K_{1,2}$ . Enlarging the twisted angle  $\Theta$  magnifies the scale of Dirac cones and broadens the two low-energy bands, but the remote bands are still separated by a sizable gap in the scale of 50 meV (see Fig. 6 in the Method).

In the 2D setting of TBG, the long-ranged single-gated

(screened) Coulomb interaction for a momentum exchange  $\mathbf{Q}$  is given as  $V(\mathbf{Q})/(4\Omega) = \frac{e^2}{16\Omega\pi\epsilon} \int d^2\mathbf{r} \left( \frac{1}{r} - \frac{1}{\sqrt{r^2+d^2}} \right) e^{i\mathbf{Q}\cdot\mathbf{r}} = e^2 (1 - e^{-|\mathbf{Q}|d}) / (8\Omega\epsilon|\mathbf{Q}|)$ , with  $\epsilon = 7\epsilon_0$ , and  $d/2 = 20$  nm the typical distance between TBG and a bottom gate [79].  $\Omega$  is the area of the total real-space moiré superlattice. Since the scale of the Coulomb interaction is less than 5 meV as  $|\mathbf{Q}| \rightarrow 0$  [43, 47], we can project the Hamiltonian from plane-wave basis to band basis considering only the two low-energy bands. Then, the Hamiltonian reads

$$H = \sum_{s,\eta,\mathbf{k},m} \epsilon_{\mathbf{k},m}^{s,\eta} c_{s,\eta,\mathbf{k},m}^\dagger c_{s,\eta,\mathbf{k},m} + \sum_{\mathbf{Q}} \frac{1}{4\Omega} V(\mathbf{Q}) (A_{\mathbf{Q}}^2 - B_{\mathbf{Q}}^2) \quad (1)$$

$$= H_0 + H_1,$$

where  $\epsilon_{\mathbf{k},m}^{s,\eta}$  is the kinetic energy for spin  $s$ , valley  $\eta$ , momentum  $\mathbf{k}$ , and band  $m$ , while  $\mathbf{Q} \neq 0$  is the momentum exchange. The interaction term contains  $A_{\mathbf{Q}} = \delta_{\rho-\mathbf{Q}} + \delta_{\rho\mathbf{Q}}$  and  $B_{\mathbf{Q}} = \delta_{\rho-\mathbf{Q}} - \delta_{\rho\mathbf{Q}}$  with the density operator

$$\delta_{\rho\mathbf{Q}} = \sum_{s,\eta,\mathbf{k},m_1,m_2} \lambda_{m_1,m_2}^{s,\eta}(\mathbf{k}, \mathbf{k} + \mathbf{Q}) \left( c_{s,\eta,\mathbf{k},m_1}^\dagger c_{s,\eta,\mathbf{k}+\mathbf{Q},m_2} - \frac{4+\nu}{8} \delta_{q,0} \delta_{m_1,m_2} \right) \quad (2)$$

and the filling factor  $\nu$ . The form factor  $\lambda_{m_1,m_2}^{s,\eta}$  comes from the projection from plane-wave basis to band basis [11, 40], see Methods for detailed derivation of Eq. (1). As shown in our previous work [43],  $V(\mathbf{Q})/(4\Omega)$  decays to almost 0 at the distance of  $|\mathbf{G}_{1,2}|$ , the module of lattice constants of mBZ, where a cutoff can be made. In the QMC simulation, we discretize the mBZ into a  $N = L \times L$  momentum grid for  $\mathbf{k}$ .

A momentum-space QMC scheme for Eq. (1) has been developed in Refs. [11, 38]. However, due to the long-range nature of the Coulomb interaction and the form factor that generates all-to-all momentum-transfer, the QMC computation for TBG suffers from a very high computational complexity of at least  $O(\beta N^4)$ , where  $\beta = 1/T$  is the inverse temperature. So, previous QMC works on TBG are all confined in relatively small systems sizes (usually up to  $L = 9$ ) and less scanning of the phase diagram in the parameter space [11, 38–43]. However, to be able to discuss the spectral properties and universality originated from the Dirac points close to the momenta  $K_{1,2}$ , one needs to be able to simulate larger system sizes and scan the twisted angle continuously, and therefore the reduction of the computational complexity becomes crucial. As pointed out in Ref. [80], the scaling can be improved by considering continuous fields and global updating schemes such as Hybrid Monte Carlo [44]. This is precisely what we have achieved in this work, as detailed in the Method section on the continuous-field Monte Carlo (CFMC). By performing the QMC simulation with continuous auxiliary fields and a global updating scheme on a single time slice, we have successfully reduced the computational complexity to  $O(\beta N^3)$ . This allows us to access a large system with  $L = 15$  at low temperature. Such large-scale QMC simulations are carried

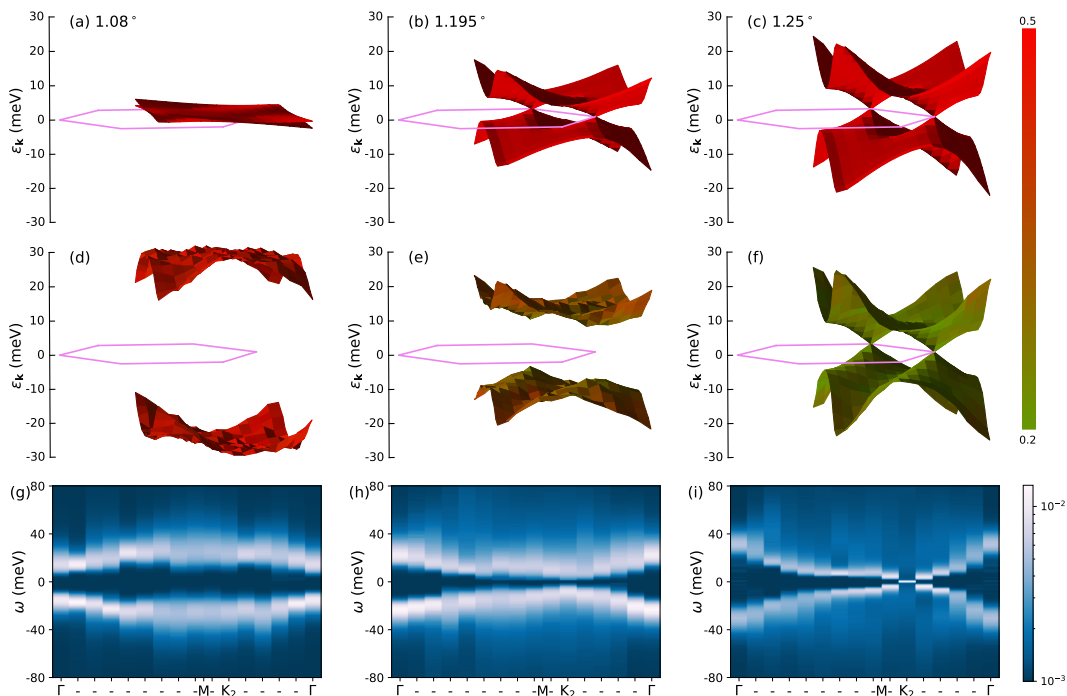


FIG. 1. **Single-particle excitation spectra as a function of the twisted angle.** The violet hexagon is the mBZ with the momentum mesh of  $15 \times 15$  in all panels, and three columns are of  $1.08^\circ$ ,  $1.195^\circ$ , and  $1.25^\circ$ , respectively. (a), (b) and (c) are the single-particle dispersion of the two low-energy bands from the continuum model without Coulomb interaction. At MA the two bands are almost flat, and the Dirac cones appear at  $K_{1,2}$  of the mBZ. (d)-(f) are the QMC obtained single-particle excitations with Coulomb interactions. They are obtained by a 2 mode approximation to the spectral function:  $A(\mathbf{k}, \omega) = -\frac{1}{\pi} \text{ImTr}G^{\text{ret}}(\mathbf{k}, \omega) \propto \sum_{m=1}^2 a_m \delta(\epsilon_m(\mathbf{k}) - \omega)$ , where the  $\epsilon_m(\mathbf{k})$  are dispersions and the  $a_m$  are the corresponding spectral weight, denoted by the color scheme. Panel (d) is at MA, where the system is gapped in the IVC state and the minima of the single-particle gaps are at the  $\Gamma$  point. QMC obtained gaps at MA are consistent with those from the exact solution [11, 47] as shown in Supplemental Material (SM) [48]. Panel (e) is at  $\Theta = 1.195^\circ$ , which is close to the  $\Theta_c$ , where the gaps close at  $K_{1/2}$  points of the mBZ, and the system is about to enter the Dirac semimetal phase through the GN-QCP. Panel (f) shows the dispersion at  $1.25^\circ > \Theta_c$ , here the Dirac dispersion is similar to that of the non-interacting counterpart in Panel (c), but with momentum-dependent weight distribution due to the Coulomb interaction. (g)-(i) Color mapping of the  $A(\mathbf{k}, \omega)$  along a high-symmetric line,  $\Gamma \rightarrow M \rightarrow K_2 \rightarrow \Gamma$ , with the twisted angles of  $1.08^\circ$ ,  $1.195^\circ$ , and  $1.25^\circ$ , respectively.

out at each  $\Theta$  that we continuously tune, and the obtained single-particle spectra, thermodynamic properties and the chiral GN quantum criticalities are what we now turn to.

### Single-Particle Spectrum, Free Energy and Criticality of the Angle-Tuned GN-QCP

In Fig. 1 we show the single-particle spectra without ((a)-(c)) and with ((d)-(i)) Coulomb interactions, where the twisted angle  $\Theta$  is tuned from the first MA at  $1.08^\circ$  to  $1.25^\circ$ . The non-interactive dispersion ((a)-(c)) is from the continuum model (see Method) and the interacting single-particle spectra ((d)-(i)) are obtained in the CFMC simulations. These spectra are obtained by a 2-mode approximation (we trace out the dynamic Green's function at each momentum point in the  $2 \times 2$  band basis) to the spectral function:  $A(\mathbf{k}, \omega) = -\frac{1}{\pi} \text{ImTr}G^{\text{ret}}(\mathbf{k}, \omega) \propto \sum_{m=1}^2 a_m \delta(\epsilon_m(\mathbf{k}) - \omega)$ , where  $G^{\text{ret}}(\mathbf{k}, \omega)$  is the single-particle Green's function from the CFMC simulation,  $\epsilon_m(\mathbf{k})$  are dispersions, and  $a_m$  is the corresponding spectral weight, denoted

by the color coding.

At the MA  $1.08^\circ$ , kinetics of TBG with the scale of 1 meV, as shown in Fig. 1 (a), is dominated by Coulomb interactions. As a result, TBG manifests a correlated insulator as its ground state [1, 4, 6, 11, 38, 39, 41, 43, 79, 81–106], as shown in Fig. 1 (d), where the QMC dispersion is consistent with exact solutions of the purely interacting Hamiltonian and previous momentum-space QMC results [11, 40, 47]. When  $\Theta$  is tuned larger away from  $1.08^\circ$ , the bandwidth for kinetic energy evolves to  $\sim 25$  meV at  $1.25^\circ$ , as shown in Fig. 1 (c), and can overwhelm the Coulomb interactions ( $< 5$  meV). In this case, even in the presence of interactions, the system is a Dirac semimetal, which is known to be stable against perturbative interactions due to the vanishing density of states at Fermi level. Indeed, we find Dirac band touching at points  $K_{1,2}$  in mBZ at this angle as shown in Figs. 1 (f). Therefore, we expect a quantum phase transition between the correlated insulator (in this case, an IVC insulator) and the Dirac semimetal. If the transition turns out to be continuous, it is a GN-QCP.

We also compute spectral functions  $A(\mathbf{k}, \omega)$  using the

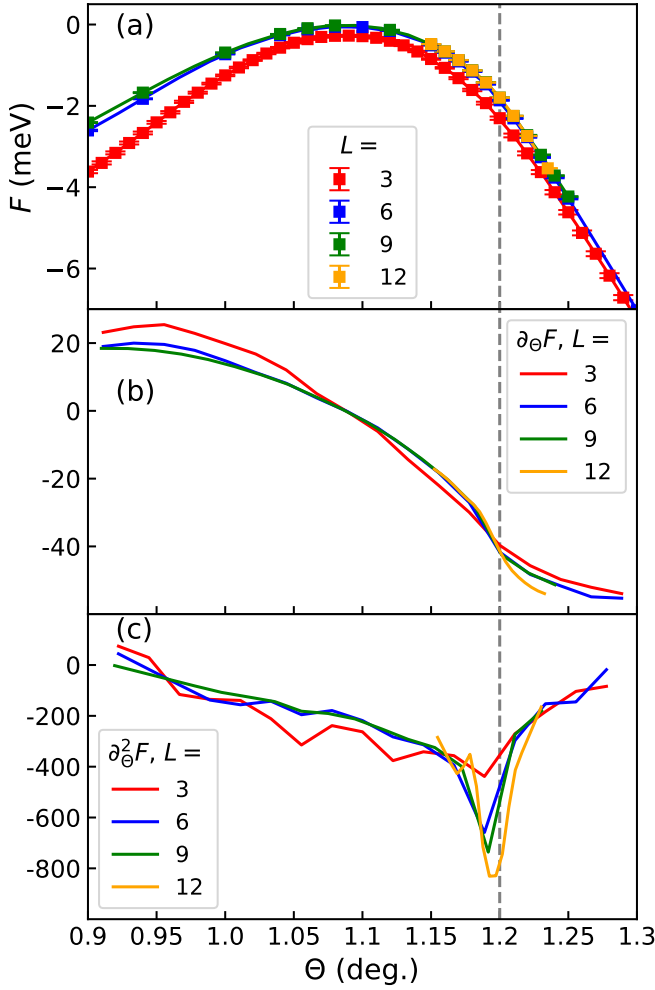


FIG. 2. **Indication of the GN-QCP from the free energy.** Free energies of  $L = 3, 6, 9,$  and  $12$  systems (with  $\beta \propto L$ ) (a) and their first- (b) and second-order (c) derivatives. The second-order derivatives exhibit divergence at  $\Theta_c \sim 1.2^\circ$  as a function of the system size, signaling a second-order phase transition between the IVC insulator and Dirac semimetal.

stochastic analytic continuation (SAC) [107, 108] of the imaginary-time Green's functions obtained in CFMC. The computational scheme is explained in detail in Methods section and here we only mention that such QMC+SAC have been successfully applied in previous momentum-space QMC simulations to reveal the ground state and finite temperature single-particle and collective excitation spectra of the TBG systems [40–43]. Our obtained spectra for the  $15 \times 15$  system are shown in Fig. 1 (g), (h) and (i), where we have chosen the high-symmetry path inside the mBZ that scans through the  $K_2$  point to highlight the different natures of the states across the transition. Fig. 1 (g) is inside the IVC state at the MA and the spectrum shows clear upper and lower Hubbard bands for the insulating ground state. Fig. 1 (h) is closer to the critical angle  $\Theta_c$  and the insulating gap is closing at the Dirac point  $K_2$ . Fig. 1 (i) is at  $1.25^\circ$  thus inside the Dirac semimetal phase,

and the linear dispersion originating from the Dirac points manifests itself. Note that the peak positions and the spectral weights of  $A(\mathbf{k}, \omega)$  are in full consistency with our 2-mode approximation in Fig. 1 (d), (e) and (f).

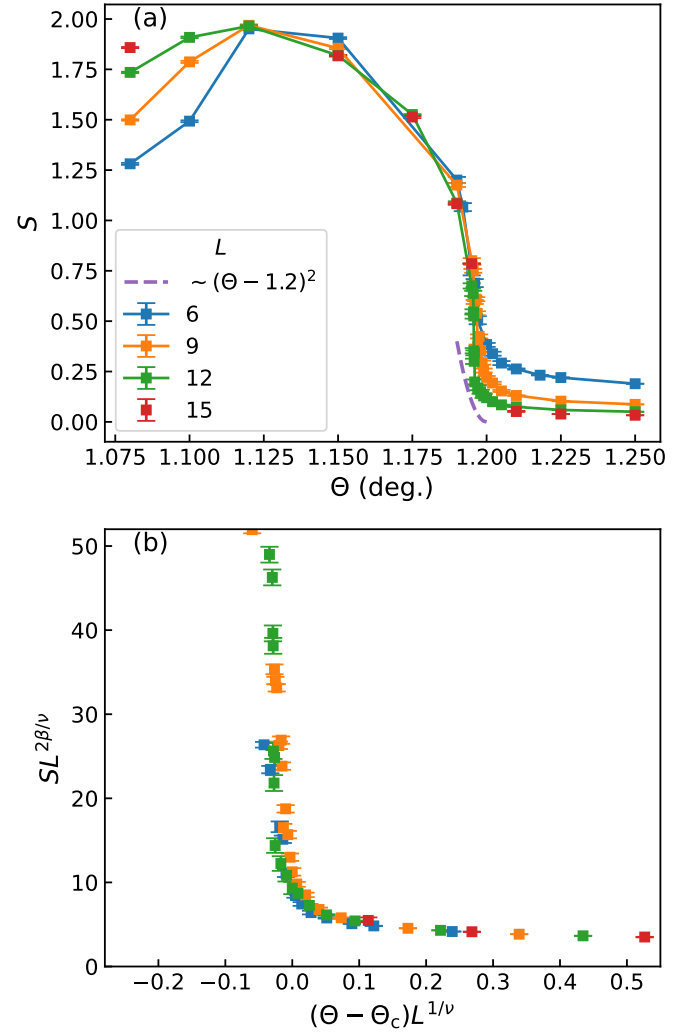


FIG. 3. **The GN-QCP analysis from the IVC order parameter.** (a) The structure factor  $S$  of IVC order parameter on the lattices with  $L = 6, 9, 12,$  and  $15$  as a function of  $\Theta$ . We set  $\beta \propto L$  in these CFMC simulations. From MA to  $1.4^\circ$ , the IVC order continuously vanishes (although there are strong finite size effect close to MA and the peak of IVC order might actually stand at  $1.08^\circ < \Theta < 1.2^\circ$ ) as the systems evolve from IVC insulator to Dirac semimetal. The dashed line is the asymptotic critical behavior of  $S \sim |\Theta - \Theta_c|^{2\beta}$ , with the  $\beta = 1.0$ . (b) With the  $N_f = 16$  chiral XY GN-QCP exponents,  $\beta = 1.0$  and  $\nu = 1.16$ , one can obtain a data collapse of  $SL^{2\beta/\nu}$  versus  $(\Theta - \Theta_c)L^{1/\nu}$  and obtain  $\Theta_c = 1.20(1)^\circ$  as the transition point. Note that within the range of  $\beta = 1.0(1)$  and  $\nu = 1.16(5)$ , almost the same good data collapse with the same  $\Theta_c$  can be achieved. This indicates the transition is indeed in the chiral XY GN universality with Dirac fermions emerging at  $\Theta > \Theta_c$ .

To locate the position and to explore the nature of the transition, we compute the free energy  $F(\Theta)$  of the system as a function of the twisted angle  $\Theta$ . The results are shown in Fig. 2.

Free energy, as one of the exponential observables [109], can be computed at finite temperature with the incremental method developed by some of us [110]. Details of the algorithm are given in Methods section. Fig. 2 (a) shows that  $F(\Theta)$  is a smooth function for  $\Theta \in [0.9^\circ, 1.3^\circ]$  (we set the inverse temperature  $\beta \propto L$  to access the ground state properties as the system size increases). Fig. 2 (b) shows that the same is also true for the derivative  $\partial F(\Theta)/\partial\Theta$ , and only the second-order derivative  $\partial^2 F(\Theta)/\partial\Theta^2$  exhibits the signature of a divergence at  $\Theta \sim 1.2^\circ$  in Fig. 2 (c). These results indicate the GN-QCP is a likely scenario and that  $\Theta_c$  is in the vicinity of  $1.2^\circ$ .

As explained in Fig. 1, the correlated insulating state in our setting is the IVC state, which breaks the U(1) symmetry of the charge conservation between the valley degrees of freedom [4, 5, 111]. Considering the two valley ( $\eta$ ), band ( $\sigma$ ), mini-valley ( $\mu$ ), and spin ( $s$ ) degrees of freedom, the Dirac semimetal at the charge neutrality point will have  $N_f = 16$  component Dirac fermions, i.e., four flavors of four-component Dirac fermions. Since the semimetal will recover the U(1) (XY) symmetry broken by the IVC insulator, an  $N_f = 16$  chiral XY GN-QCP is expected. The effective action describing this universality class is given by

$$\mathcal{L} = \int \frac{d^3k}{(2\pi)^3} \psi^\dagger (-i\omega + \sigma_z |k|) \psi + \int d^3x \left[ \frac{1}{2} \phi (\partial_x^2 + \partial_y^2) \phi + \frac{1}{2} m^2 \phi^2 + \frac{1}{4} \lambda \phi^4 + g \phi^a \psi^\dagger M_a \psi \right] \quad (3)$$

where  $\psi$  and  $\phi$  denote the fermionic and bosonic (order) parameter field and  $a$  the components of  $\phi$ . The 16-component, low-energy fermion spinor  $\psi_{\mathbf{k}} = (c_{s,\eta,K_1+\mathbf{k},m}, c_{s,\eta,K_2+\mathbf{k},m})^\top$  is obtained by expanding fermion modes around the mini-valley  $K_{1,2}$  points. In our case, for the chiral XY phase transition,  $M_1 = \eta_x \sigma_y$  and  $M_2 = \eta_y \sigma_x$ .

The consistency to a chiral XY GN-QCP is verified from the IVC order parameter computed in QMC simulation. According to Eq. (1), it is defined as  $O \equiv \sum_{s,\mathbf{k}} \vec{c}_{s,\mathbf{k}+\mathbf{q}}^\dagger \eta_x \sigma_y \vec{c}_{s,\mathbf{k}} = \sum_{s,\eta,\mathbf{k},m} i m c_{s,\eta,\mathbf{k}+\mathbf{q},m}^\dagger c_{s,-\eta,\mathbf{k},-m}$  or  $\sum_{s,\mathbf{k}} \vec{c}_{s,\mathbf{k}+\mathbf{q}}^\dagger \eta_y \sigma_x \vec{c}_{s,\mathbf{k}} = \sum_{s,\eta,\mathbf{k},m} -\eta m c_{s,\eta,\mathbf{k}+\mathbf{q},m}^\dagger c_{s,-\eta,\mathbf{k},-m}$  with  $(\eta_x, \eta_y)$  and  $\sigma_y$  Pauli matrices for valley and band indices [5, 38, 41] when the entire continuum dispersion is included. The correlation function of IVC at its ordered wavevector  $\Gamma$ ,  $S = \langle O^\dagger O \rangle / N^2$  as a function of  $\Theta$ , is shown in Fig. 3 (a). The order at MA has been intensively studied [4, 5, 46, 111], and it is known by now that due to the presence of kinetic energy with  $u_0 = 60$  meV, the IVC order is the leading instability compared with valley polarized order [38, 41]. From our data in Fig. 3 (a), it is clear that the IVC order is strong at  $\Theta < 1.2^\circ$ , we even find that there is a substantial finite-size dependence in the value of  $S$  at the MA, which might indicate the strongest IVC order at slightly larger angles than the MA. As the twisted angle increases further, the IVC order vanishes around  $1.2^\circ$  in a steep but continuous way, which is consistent with the free-energy behaviour within our resolution for  $\Theta$  angles.

To check consistency of the QMC data with the critical exponents of the  $N_f = 16$  chiral XY GN-QCP, we calculate the inverse correlation length exponent  $\nu^{-1}$  and the anomalous dimension of the order parameter field  $\eta$ . Accurate results can be obtained by expanding around the upper critical (space-time) dimension  $D = 4 - \epsilon$ . We use the results of a four-loop  $\epsilon$ -expansion [70] and average over different Padé approximants for the dimensional dependence (details of the calculation is given in the Methods). We then employ the hyperscaling relation to determine the scaling exponent of the order parameter  $\beta = \nu(D - 2 - \eta)/2$ . We find  $\nu = 1.13$  and  $\beta = 1.09(5)$ . Furthermore, within the four-loop  $\epsilon$ -expansion, we are able to calculate the correction-to-scaling exponent  $\omega$ , which corresponds to an  $L^{-\omega}$  term in the scaling function of the order parameter. We find that for  $N_f = 16$ ,  $\omega = 0.862(1)$ . For comparison  $\omega = 0.788(8)$  for the same universality class in monolayer graphene, which corresponds to  $N_f = 8$ . As such, we expect these corrections to be negligible due to the larger number of fermion flavours that are present in TBG.

One can already see from Fig. 3 (a), that the dashed line is the asymptotic critical behavior of  $S \sim |\Theta - \Theta_c|^{2\beta}$ , with the  $\beta = 1.0$ . Our finite-size data is approaching the asymptotic behavior as  $L$  increases. In Fig. 3 (b), we performed the finite size analysis to collapse our data with  $\beta = 1.0$  and  $\nu = 1.16$ . The obtained  $\Theta_c = 1.20(1)^\circ$ . We note that within the range of  $\beta = 1.0(1)$  and  $\nu = 1.16(5)$ , almost the same good data collapse with the same  $\Theta_c$  can be achieved. These results demonstrate the consistency of the chiral XY GN-QCP with the position and the nature of the transition in TBG as indicated in the single-particle spectrum and free energy. We note that such consistency is only made possible because the CFMC allows for larger system sizes (up to  $L = 15$ ). Otherwise, it is impossible to access this information with the discretized-field version of momentum-space QMC in which the largest system size is  $L = 9$ . In the SM [48], we also show the same data analyzed with the (2+1)D XY exponents  $\beta = 0.35$ ,  $\nu = 0.67$  [112, 113], and the data collapse is less satisfactory. This reinforces the understanding that the transition we observe is non-thermal and involves the Dirac fermions, i.e., it is of GN-type.

## DISCUSSION

With the development of CFMC numerical method, we succeeded in discovering the angle-tuned quantum critical point in pristine TBG at charge-neutrality which separates semi-metallic Dirac electrons from a gapped phase with K-IVC order. Such an interaction-driven transition was not possible to realize in other systems, e.g., in graphene because the interaction is too weak. Therefore, we offer the new and exciting opportunity that if one can continuously tune the angle from the magic one ( $1.08^\circ$ ) to  $1.25^\circ$ , a quantum critical point with novel critical behavior and an emergent Dirac semimetal can be seen from pristine TBG.

We showed that tuning the angle manipulates the band struc-

ture and interaction of the narrow bands. As the twisted angle increases, the Coulomb interactions effectively become weaker when being compared to kinetics, while remote bands remain well separated. This has a strong effect on the single-particle excitations in TBG. When  $\Theta < \Theta_c$ , we find the single-particle bands are well approximated by an exact solution of the purely interacting model with a minimum at  $\Gamma$  at the magic angle  $\Theta = 1.08^\circ$ . However, the spectrum changes qualitatively as a function of the angle towards Dirac dispersion with touching points at  $K_{1,2}$  for  $\Theta > 1.20^\circ$ . During the evolution, we observe a redistribution of the spectral weight from high-energy modes towards the low-energy Dirac cones. As an interesting by-product, we notice that the critical region is small in terms of the control parameter  $\Theta$ . Our understanding is that the projected Coulomb repulsion generates many possible mass terms that compete. This is reminiscent of single layer graphene with unscreened Coulomb repulsion where both Charge Density Wave (CDW) and antiferromagnetic (AFM) orders are strong [114] and similar behavior of a narrower window of the transition point has been observed [115, 116].

In terms of quantum many-body computation, it is well-known that progress in numerical simulations of TBG is important, and the momentum-space QMC and its CFMC improvement implemented in this work are substantial developments. The usage of such QMC algorithm can be even broader. In fact, the algorithms for TBG are identical to those used in the realm of Landau level regularisations schemes for continuum field theories, let it be on the torus [80, 117] or on the sphere [118, 119]. Also our CFMC method will have potential applications in  $\text{MoTe}_2$  and multilayer graphene systems where the fractional quantum anomalous Hall effects have recently been seen [120–123]. In TBG and other 2D quantum moiré systems, the interplay of the long-range Coulomb interactions and the quantum metric of flat bands must be considered with equal footing, and our approach paves the way to achieve this and simulate larger system sizes.

At the fundamental level, our proposal of a realisation in TBG is more generally relevant for the study of interaction-induced phase transitions in Dirac semi-metals. Close to the transition, the emergent quantum critical behavior is universal. We demonstrated that the critical behaviour in TBG is consistent with the Gross-Neveu chiral XY universality class with emergent Lorentz invariance. The Gross Neveu model describes the spontaneous mass generation of relativistic Dirac electrons, and can be taken as an effective low-energy model for the chiral phase transition of QCD. In the condensed matter context, its quantum phase transition was studied extensively via different theoretical methods such as QMC [54–72, 124, 125], bootstrap [66, 126], and renormalisation group [59, 70, 127–129], and critical exponents are beginning to converge. In this sense, it can be seen as the minimal model for fermionic quantum critical transitions, analogous to the  $O(N)$  model at thermal phase transitions. Thus, the experimental realisation in a highly-tunable platform like TBG promises the possibility to simulate, on the one hand, a standard model for fermionic quantum criticality, and on

the other hand, the spontaneous mass generation during chiral symmetry breaking in two dimensions.

Experimentally, *in-situ* tuning of the twist angle has recently become possible, e.g., via a quantum twisting microscope [7], or manipulation via microscopic handles [35–37]. Furthermore, information on the twist-angle dependence of single-particle spectrum can be obtained from different domains in STM measurements. The presence of Dirac electrons and their velocity renormalisation with twist angle can be measured via quantum oscillations. A spectral gap can be extracted from transport, STM and quantum capacitance experiments, which can also help to infer different symmetry breaking due to interaction. In this context, it is important to note that strain has a strong effect on the spectrum and can drive the system back into the semimetallic state. It will be interesting to study further how it affects the quantum critical behavior.

## Methods

### Continuum model of angle-twisted TBG.

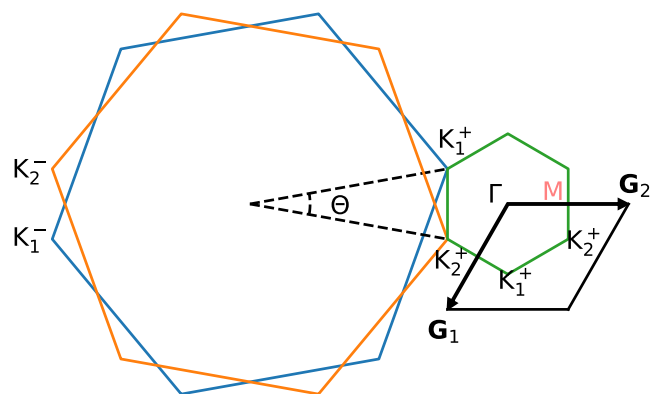


FIG. 4. **Momentum-space configuration of BZs and mBZs.** Twisting of graphene BZs as blue and orange hexagon leads to the mBZs as green hexagon or black rhombus with lattices of  $\mathbf{G}_1$  and  $\mathbf{G}_2$ .  $\Theta$  is the twisted angle and  $K_l^\eta$  is a Dirac point of valley  $\eta$  and layer  $l$ .  $\Gamma$  and  $M$  are two high-symmetric points.

The schematic twisting of graphene Brillouin zone and corresponding moiré Brillouin zone are drawn in Fig. 4. The length of the lattice vectors of mBZ is  $|\mathbf{G}_1|, |\mathbf{G}_2| = 8\pi\sin(\Theta/2)/(3a)$  with  $a = 1.42\text{\AA}$  being the distance between nearest carbon atoms.  $K_1^\eta$  and  $K_2^\eta$  are Dirac points of valley  $\eta = \pm$  from the top (1) and bottom (2) layers, respectively. A momentum-space single-particle Hamiltonian,  $H_0$ , considering intralayer hopping and interlayer hopping, can be constructed as

$$H_0 = \sum_{s,\eta,\mathbf{k},G,X,G',X'} c_{s,\eta,\mathbf{k},G,X}^\dagger H^{s,\eta}(\mathbf{k})_{G,X,G',X'} c_{s,\eta,\mathbf{k},G',X'}. \quad (4)$$

Here

$$\begin{aligned}
& H^{s,\eta}(\mathbf{k})_{\mathbf{G},\mathbf{G}'} \\
&= \delta_{\mathbf{G},\mathbf{G}'} \hbar v_F \begin{pmatrix} -(\mathbf{k} + \mathbf{G} - \mathbf{K}_1^\eta) \cdot \boldsymbol{\Lambda}^\eta & 0 \\ 0 & -(\mathbf{k} + \mathbf{G} - \mathbf{K}_2^\eta) \cdot \boldsymbol{\Lambda}^\eta \end{pmatrix} \\
&+ \begin{pmatrix} 0 & T_1^{\eta\dagger} \\ T_2^{\eta\dagger} & 0 \end{pmatrix}
\end{aligned} \quad (5)$$

is the BM model [18] with

$$\begin{aligned}
T_l^\eta &= \begin{pmatrix} u_0 & u_1 \\ u_1 & u_0 \end{pmatrix} \delta_{\mathbf{G},\mathbf{G}'} + \begin{pmatrix} u_0 & u_1 e^{-i\frac{2\pi}{3}\eta} \\ u_1 e^{i\frac{2\pi}{3}\eta} & u_0 \end{pmatrix} \delta_{\mathbf{G},\mathbf{G}'+(-1)^l \eta \mathbf{G}_1} \\
&+ \begin{pmatrix} u_0 & u_1 e^{i\frac{2\pi}{3}\eta} \\ u_1 e^{-i\frac{2\pi}{3}\eta} & u_0 \end{pmatrix} \delta_{\mathbf{G},\mathbf{G}'+(-1)^l \eta (\mathbf{G}_1 + \mathbf{G}_2)}.
\end{aligned} \quad (6)$$

$\mathbf{k}$  is a momentum in mBZ,  $\mathbf{G}$  and  $\mathbf{G}'$  are momentum differences for  $\mathbf{k}$  to account for the contribution from extended Brillouin zones. Vectors  $\mathbf{G}, \mathbf{G}' \in \{n_1 \mathbf{G}_1 + n_2 \mathbf{G}_2\}$  define the lattice of mBZs, with  $n_1$  and  $n_2$  being integers, and a cutoff,  $|\mathbf{G}|, |\mathbf{G}'| \leq 6|\mathbf{G}_1|$ , is applied.  $c_{s,\eta,\mathbf{k},\mathbf{G},X}^\dagger$  is the creation operator of an electron with spin  $s = \uparrow, \downarrow$ , valley  $\eta = \pm$ , momentum  $\mathbf{k}$ , and layer and sublattice  $X \in \{1A, 1B, 2A, 2B\}$  for layers (1, 2) and sublattices (A, B).  $v_F$  is the Fermi velocity and  $\hbar v_F / (\sqrt{3}a) = 2.37745$  eV.  $\boldsymbol{\Lambda}^\eta = (\eta \Lambda_x, \eta \Lambda_y)$ , where  $\Lambda_x$  and  $\Lambda_y$  are Pauli matrices in sublattice space. The first part of  $H^{s,\eta}(\mathbf{k})_{\mathbf{G},\mathbf{G}'}$  stands for intra-layer hopping of the top (1) layer and the bottom (2) layer, respectively, and the second part stands for inter-layer hopping with  $u_0 = 0.06$  eV and  $u_1 = 0.11$  eV, which is actually the moiré potential.

The dispersion of  $H_0$  for several twisted angles are shown in Fig. 5, where enlarging of the bandwidth of two low-energy bands is seen with departing  $\Theta$  from MA. As the lower bands are always isolated from the remote bands by  $\sim 50$  meV and the screened Coulomb potential is maximally 5 meV [43], the low-energy physics can be well captured by these two low-energy bands.

The single-gated Coulomb interaction after Fourier's transformation is

$$H_1 = \frac{1}{2\Omega} \sum_{\mathbf{q} \in \text{mBZ}, \mathbf{G}} V(\mathbf{q} + \mathbf{G}) \delta \rho_{\mathbf{q}+\mathbf{G}} \delta \rho_{-\mathbf{q}-\mathbf{G}}, \quad (7)$$

where

$$\begin{aligned}
& \delta \rho_{\mathbf{q}+\mathbf{G}} \\
&= \sum_{s,\eta,\mathbf{k},\mathbf{G}',X'} \left( c_{s,\eta,\mathbf{k},\mathbf{G}',X'}^\dagger c_{s,\eta,\mathbf{k}+\mathbf{q}+\mathbf{G},\mathbf{G}',X'} - \frac{\nu+4}{8} \delta_{\mathbf{q},0} \delta_{\mathbf{G},0} \right).
\end{aligned} \quad (8)$$

Here  $\delta \rho_{\mathbf{q}+\mathbf{G}}$  is the electron density operator with respect to  $(\nu+4)/8$  filling, and  $\nu$  is the filling parameter with  $\nu = 0$  corresponding to the charge neutrality.  $\Omega = N |\mathbf{a}_{M1}| |\mathbf{a}_{M2}| \sqrt{3}/2$  is the total area of moiré superlattice in real space, and  $\mathbf{a}_{M1}$  and  $\mathbf{a}_{M2}$  are the lattice vectors of real-space unit cell of superlattice with  $|\mathbf{a}_{M1/M2}| = \sqrt{3}a / [2\sin(\Theta/2)]$ .

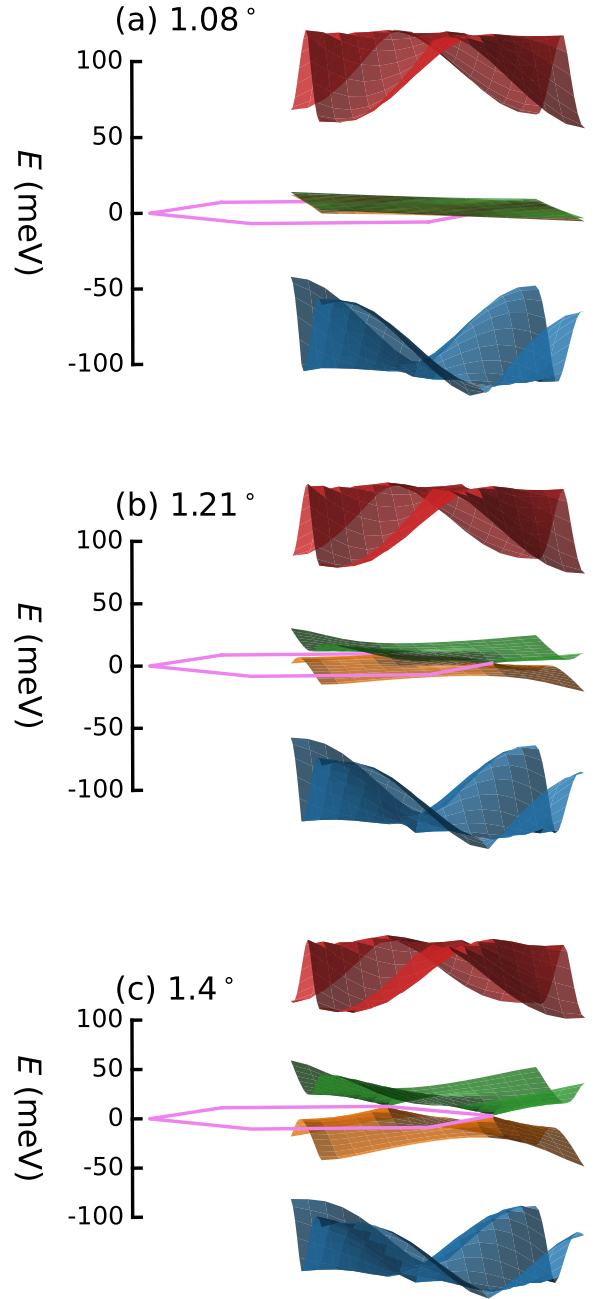


FIG. 5. **Four low-energy bands for  $L = 15$  without Coulomb interaction.** (a)  $1.08^\circ$ , (b)  $1.21^\circ$ , and (c)  $1.4^\circ$ . Note that the mBZ is denoted by the violet hexagon. The two low-energy bands are also shown in Fig. 1 (a), (b) and (c) in the main text.

We denoting the eigenvalues and eigenvectors of  $H^{s,\eta}(\mathbf{k})$  as  $\epsilon_{k,m}^{s,\eta}$  and  $|u_{k,m}^{s,\eta}\rangle$ . Then  $H_0$  and  $H_1$  can be projected to band basis as

$$H_0 = \sum_{s,\eta,k,m} \epsilon_{k,m}^{s,\eta} c_{s,\eta,k,m}^\dagger c_{s,\eta,k,m}, \quad (9)$$

and

$$H_1 = \frac{1}{2\Omega} \sum_{|\mathbf{q}+\mathbf{G}|\neq 0} V(\mathbf{q}+\mathbf{G}) \delta\rho_{\mathbf{q}+\mathbf{G}} \delta\rho_{-\mathbf{q}-\mathbf{G}}, \quad (10)$$

with  $c_{s,\eta,k,m}^\dagger = \sum_{G,X} c_{s,\eta,k,G,X}^\dagger |u_{k,m}^{s,\eta}\rangle_{G,X}$  and  $\delta\rho_{\mathbf{q}+\mathbf{G}} = \sum_{s,\eta,k,m_1,m_2} \lambda_{m_1,m_2}^{s,\eta} (\mathbf{k}, \mathbf{k} + \mathbf{q} + \mathbf{G}) \left( c_{s,\eta,k,m_1}^\dagger c_{s,\eta,k+\mathbf{q}+\mathbf{G},m_2} - \frac{\nu+4}{8} \delta_{\mathbf{q},0} \delta_{m_1,m_2} \right)$ . The form factor is defined as  $\lambda_{m_1,m_2}^{s,\eta} (\mathbf{k}, \mathbf{k} + \mathbf{q} + \mathbf{G}) \equiv \langle u_{\mathbf{k},m_1}^{s,\eta} | u_{\mathbf{k}+\mathbf{q}+\mathbf{G},m_2}^{s,\eta} \rangle$ . Since the low-energy physics can be well approximated by the two low-energy bands,  $m$  index has now only two possible values:  $m = \pm$ . Introducing the notation  $\mathbf{Q} = \mathbf{q} + \mathbf{G}$ ,  $H_1$  can be rewritten as

$$\begin{aligned} H_1 &= \sum_{|\mathbf{Q}|\neq 0} \frac{1}{2\Omega} V(\mathbf{Q}) \delta\rho_{\mathbf{Q}} \delta\rho_{-\mathbf{Q}} \\ &= \sum_{\mathbf{Q}} \frac{1}{2\Omega} V(\mathbf{Q}) (\delta\rho_{\mathbf{Q}} \delta\rho_{-\mathbf{Q}} + \delta\rho_{-\mathbf{Q}} \delta\rho_{\mathbf{Q}}) \\ &= \sum_{\mathbf{Q}} \frac{1}{4\Omega} V(\mathbf{Q}) \left( (\delta\rho_{-\mathbf{Q}} + \delta\rho_{\mathbf{Q}})^2 - (\delta\rho_{-\mathbf{Q}} - \delta\rho_{\mathbf{Q}})^2 \right) \\ &= \sum_{\mathbf{Q}} \frac{1}{4\Omega} V(\mathbf{Q}) \left( A_{\mathbf{Q}}^2 - B_{\mathbf{Q}}^2 \right). \end{aligned} \quad (11)$$

Note that  $\delta\rho_{\mathbf{Q}} \delta\rho_{-\mathbf{Q}}$  is written as  $\delta\rho_{\mathbf{Q}} \delta\rho_{-\mathbf{Q}} + \delta\rho_{-\mathbf{Q}} \delta\rho_{\mathbf{Q}}$  in the second line of Eq. 11, so that we sum over half of the possible  $\mathbf{Q}$  values with the additional condition  $\{|\mathbf{Q}| \neq 0\}$  [11].  $H_0$  in Eq. (9) and  $H_1$  in the Eq. (11) are exactly the terms used in the Hamiltonian (1) in the main text.

### The CFMC algorithm

The Hamiltonian in Eq. (1) has been solved with momentum-space QMC method with discretized auxiliary fields [11]. Similar to other determinantal QMC methods, it applies the Hubbard-Stratonovich transformation to decouple the Coulomb interaction, following the Trotter decomposition [130–134]. Due to  $C_{2z}P$  symmetry the system at charge neutrality is free of sign problem [11]. The simulation temperature is set to be  $1/T \sim L$  with  $T = 1$  meV for  $L = 3$ , and decreasing with increasing  $L$ .

Original version of the momentum-space QMC method uses the discrete version of the Hubbard-Stratonovich transformation:

$$\begin{aligned} \exp(-\alpha_1(\mathbf{Q}) A_{\mathbf{Q}}^2) &= \frac{1}{4} \sum_{l_{\mathbf{Q},1}} \gamma(l_{\mathbf{Q},1}) \exp\left(i\xi(l_{\mathbf{Q},1}) \sqrt{\alpha_1(\mathbf{Q})} A_{\mathbf{Q}}\right) \\ &\quad + \mathcal{O}(\Delta\tau^4), \end{aligned} \quad (12)$$

and

$$\begin{aligned} \exp(\alpha_1(\mathbf{Q}) B_{\mathbf{Q}}^2) &= \frac{1}{4} \sum_{l_{\mathbf{Q},2}} \gamma(l_{\mathbf{Q},2}) \exp\left(\xi(l_{\mathbf{Q},2}) \sqrt{\alpha_1(\mathbf{Q})} B_{\mathbf{Q}}\right) \\ &\quad + \mathcal{O}(\Delta\tau^4). \end{aligned} \quad (13)$$

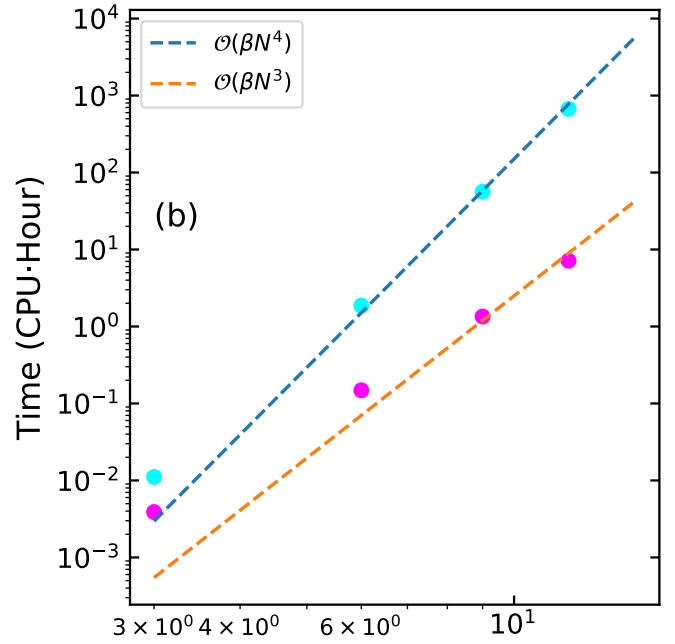


FIG. 6. **Computational complexities of DQMC and CFMC with the same physical settings.** We measure the CPU time consumed for 100 sweeps in the units of CPU core hours. Note that inverse temperature also scales with the systems size:  $\beta \sim L$ . The data can be very well described by the fits of  $\beta N^4$  and  $\beta N^3$  for DQMC and CFMC respectively, especially in the limit of large system size.

Here  $l_{\mathbf{Q},1(2)} = \pm 1, \pm 2$  is a discrete auxiliary field, and the coefficients,  $\gamma(\pm 1) = 1 + \sqrt{6}/3$ ,  $\gamma(\pm 2) = 1 - \sqrt{6}/3$ ,  $\xi(\pm 1) = \pm\sqrt{6 - 2\sqrt{6}}$ , and  $\xi(\pm 2) = \pm\sqrt{6 + 2\sqrt{6}}$  are taken from the eighth order approximation in [132].  $\alpha_1(\mathbf{Q}) = \Delta\tau V(\mathbf{Q})/4\Omega$  since the imaginary time  $\beta = 1/(k_B T)$  is evenly sliced into  $N_\tau$  pieces, as  $\Delta\tau = \beta/N_\tau$ . The partition function,  $Z = \text{Tr}\{\exp(-\beta H)\}$ , yields

$$Z = \sum_{\{l_{\tau,\mathbf{Q},1}, l_{\tau,\mathbf{Q},2}\}} \text{Tr}\{U_C\} \quad (14)$$

with

$$\begin{aligned} U_C &= \prod_{\tau=\Delta\tau}^{\beta} \exp(-\Delta\tau H_0) \prod_{\mathbf{Q}} \frac{1}{16} \gamma(l_{\tau,\mathbf{Q},1}) \gamma(l_{\tau,\mathbf{Q},2}) \\ &\quad \times \exp\left(i\xi(l_{\tau,\mathbf{Q},1}) \sqrt{\alpha_1(\mathbf{Q})} A_{\mathbf{Q}}\right) \\ &\quad \times \exp\left(\xi(l_{\tau,\mathbf{Q},2}) \sqrt{\alpha_1(\mathbf{Q})} B_{\mathbf{Q}}\right) \\ &\quad + \mathcal{O}(\Delta\tau^2). \end{aligned} \quad (15)$$

With the partition function at hand, measurements can be done by sampling the discrete auxiliary fields with the Metropolis-Hastings scheme. Local update of one auxiliary field  $l_{\mathbf{Q},1(2)}$  yields an acceptance rate around 0.4 and cluster update of multiple fields have a vanishing accepting rate. The simulation has no sign-problem at charge-neutrality  $\nu = 0$  while a unique polynomial sign-problem at other integer fillings was reported



in [39, 135]. Due to the coupling of auxiliary field to non-local operators  $A_{\mathbf{Q}}$  and  $B_{\mathbf{Q}}$ , each local update of the fields  $l_{\tau, \mathbf{Q}, 1(2)}$  leads to the computation of matrix determinant with the complexity  $O(N^3)$ . Combining with the absence of the efficient cluster update scheme for discrete fields, it leads to the overall scaling of the original momentum-space QMC of at least  $O(\beta N^4)$ . This is substantially worse than the conventional determinantal QMC scaling of  $O(\beta N^3)$  [132]. Therefore, the previous studies were heavily constrained in the accessible system sizes with the largest one being  $L = 9$  [38, 41].

To reduce the computational complexity, we develop a continuous-field Monte Carlo (CFMC) scheme to carry out cluster updates of multiple auxiliary fields at once. First of all, we switch to continuous auxiliary fields using the Gaussian integrals

$$e^{\frac{1}{2} \alpha_2 A^2} = \frac{1}{\sqrt{2\pi}} \int_{-\infty}^{\infty} d\phi e^{-\frac{1}{2} \phi^2} e^{-\phi \sqrt{\alpha_2} A}, \quad (16)$$

to rewrite the partition function in Eq. (14) in the form

$$\begin{aligned} Z = & \int \prod_{\tau, \mathbf{Q}} d\phi_{\tau, \mathbf{Q}, 1} d\phi_{\tau, \mathbf{Q}, 2} e^{-\frac{1}{2} \sum_{\tau, \mathbf{Q}} (\phi_{\tau, \mathbf{Q}, 1}^2 + \phi_{\tau, \mathbf{Q}, 2}^2)} \\ & \times \text{Tr} \left( \prod_{\tau} e^{-\Delta\tau H_0} e^{i \sum_{\mathbf{Q}} (-\phi_{\tau, \mathbf{Q}, 1} \sqrt{\alpha_2(\mathbf{Q})} A_{\mathbf{Q}} + i \phi_{\tau, \mathbf{Q}, 2} \sqrt{\alpha_2(\mathbf{Q})} B_{\mathbf{Q}})} \right) \\ & + O(\Delta\tau^2), \end{aligned} \quad (17)$$

where  $\alpha_2(\mathbf{Q}) = \Delta\tau V(\mathbf{Q})/2\Omega$ . In general, we employ the same scheme Metropolis-Hastings scheme for the updates of the continuous fields  $\phi_{\tau, \mathbf{Q}, 1(2)}$ , using Gaussian distribution as a proposal one. Unlike the discrete fields from Eqs. (12) and (13), it allows for more efficient cluster updates since the width of the proposal distribution can be tuned continuously. Small width would make an acceptance rate around one while a bold move would lead to a vanishing acceptance rate, similar to the discrete case. Here we tune the width to make the acceptance rate around 0.4. It means that the difference between new and old value of the auxiliary field is written as  $\Delta\phi_{\tau, \mathbf{Q}, 1(2)} = rx$  with  $r$  being the control parameter and  $x$  generated from a standard normal distribution,  $\mathcal{N}(0, 1)$ . We can subsequently alter  $r$  by setting  $r \rightarrow r + (R_a - 0.4)\Delta r$  where  $\Delta r$  is a tuning constant and  $R_a$  is the measured acceptance rate.  $R_a$  smaller than 0.4 means  $\Delta\phi_{\tau, \mathbf{Q}, 1(2)}$  are larger than the desirable ones, thus  $r$  is decreased, and vice versa.  $R_a \sim 0.4$  should be achieved before the Markov process reaches equilibrium distribution.

In practice we update the whole cluster of  $\phi_{\tau, \mathbf{Q}, 1(2)}$  fields at a specific  $\tau$ . The number of auxiliary fields in this cluster is  $2N_{\mathbf{Q}} \sim 3N$  (the cutoff at  $|\mathbf{G}_1|$  makes the number of momentum exchanges roughly 3 times of the number of  $\mathbf{k}$  points in mBZ), and we need only one calculation of matrix determinant with complexity  $O(N^3)$  for this update. Thus the overall complexity of the algorithm is reduced by a factor of  $O(2N_{\mathbf{Q}})$ .

The full protocol of CFMC can be described as follows

1. Generating all  $\phi_{\tau, \mathbf{Q}, 1(2)}$  fields in a cluster using normal distribution  $\mathcal{N}(0, 1)$  and current value of  $r$  parameter (initially we set  $r$  and  $\Delta r$  to 0.1).

2. Computation of the ratio of fermionic determinants before and after the update and accept-reject step according to Metropolis-Hastings scheme.
3. Repeating the updates for all time slices from 0 to  $\beta$  then reversely to complete a full sweep through the lattice. Then we compute accept ratio  $R_a$  and alter  $r$  using the rule  $r \rightarrow r + (R_a - 0.4)\Delta r$ .
4. Repeating the sweeps until sufficient statistics is gained for all observables.

Since the auxiliary fields are continuous, it is easy to adopt more sophisticated updating schemes like Hamiltonian dynamics to improve the proposal distribution [44, 115, 136]. We also note that our CFMC algorithm can be applied not only to TBG but also to other systems with long-range interaction where the local update of discrete auxiliary field is at least  $O(N)$  times more expensive due to coupling of auxiliary field to fermionic bilinear with dense matrix in momentum or configuration space. One example of such system is the projected half-filled Landau level which maps to the (2+1)D SO(5) nonlinear sigma model with Wess-Zumino-Witten term [80, 117, 119, 137, 138].

Comparison of performance of CFMC and discrete QMC (DQMC) algorithms is shown in Fig. 6 using the same physical settings for both cases. We can clearly see that CFMC indeed reduces the computational complexity from  $O(\beta N^4)$  to  $O(\beta N^3)$ , since the CPU time consumed by DQMC grows much faster than the one by CFMC, as system size increases.

The CPU time per update is not the only metric which defines the performance of the Monte Carlo scheme. It can be that different updates lead to substantially different distributions of the observables (despite the average values being fixed) [139]. Thus, the faster algorithm can potentially suffer from larger statistical fluctuations, which can even cancel the gain in the speed of update. In order to check this, we plot the Monte Carlo time series of the IVC structure factor from DQMC and CFMC simulations. Results for  $\Theta = 1.08^\circ, 1.2^\circ, \text{ and } 1.3^\circ$  are shown in Fig. 7. The histograms for the time series are drawn on top of them using the red and blue lines. The overlap of histograms indicates that fluctuations of DQMC and CFMC are very similar, thus the overall increase in performance from  $O(\beta N^4)$  scaling to  $O(\beta N^3)$  scaling still holds.

Finally, we also compare autocorrelation times for the CFMC and DQMC methods (see Fig. 8). Since the measurements are done after updates of the fields in each time slice, we compare autocorrelation times for measurements separated by a Euclidean time interval  $\Delta t$ . The autocorrelation time definitely increases for CFMC. However, it only compensates the factor  $N$  speedup at MA and the smallest lattice size. Once we go away from  $L = 6$  and  $\Theta = 1.08^\circ$ , the difference in scaling between  $O(\beta N^4)$  and  $O(\beta N^3)$  more than compensates the prefactor stemming from increased autocorrelation time. Thus we conclude that CFMC indeed substantially increases the performance of the Monte Carlo simulations.

### Stochastic analytic continuation

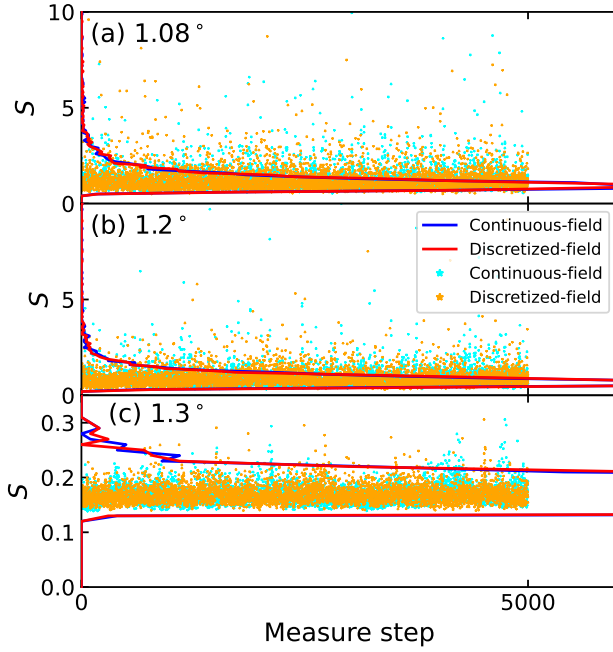


FIG. 7. **Time series of the IVC structure factor between DQMC and CFMC.** The time series of the IVC structure factor for  $L = 6$  from DQMC and CFMC as orange stars and cyan stars respectively, and corresponding histograms as red line and blue line respectively are shown, where (a) is of  $1.08^\circ$ , (b) is of  $1.2^\circ$ , and (c) is of  $1.3^\circ$ . Note that the y scales in (c) is different.

We employ the stochastic analytic continuation (SAC) [40–43, 107, 108] method to extract the real frequency spectral functions. The Green’s function is related to the real frequency spectral function as [41]

$$G(\mathbf{k}, \tau) = \int_{-\infty}^{\infty} d\omega \left( \frac{e^{-\omega\tau}}{1 + e^{-\beta\omega}} \right) A(\mathbf{k}, \omega). \quad (18)$$

A variational ansatz of  $A(\mathbf{k}, \omega)$  simulating an annealing process is applied. For each momentum  $\mathbf{k}$ ,  $A(\omega) = \sum_{i=1}^{N_\omega} A_i \delta(\omega - \omega_i)$  where frequencies  $\omega_i$  initially form regular grid with length of  $0.5k_B T$  of  $N_\omega = 4000$  points symmetrically distributed around 0. Then  $A(\omega)$  is estimated by sampling over the grids  $(A_i, \omega_i)$ , using Eq. 18 and the effective action

$$\chi^2 = \sum_{\tau_1, \tau_2} \left( \overline{G}(\tau_1) - \int_{-\infty}^{\infty} d\omega \left( \frac{e^{-\omega\tau}}{1 + e^{-\beta\omega}} \right) A(\omega) \right) (C^{-1})_{\tau_1, \tau_2} \times \left( \overline{G}(\tau_2) - \int_{-\infty}^{\infty} d\omega \left( \frac{e^{-\omega\tau}}{1 + e^{-\beta\omega}} \right) A(\omega) \right), \quad (19)$$

where

$$C_{\tau_1, \tau_2} = \frac{1}{N_b(N_b - 1)} \sum_{b=1}^{N_b} \left( G^b(\tau_1) - \overline{G}(\tau_1) \right) \left( G^b(\tau_2) - \overline{G}(\tau_2) \right), \quad (20)$$

with  $\tau_1$  and  $\tau_2$  referring to selected imaginary times where the errors of Green’s functions are less than 0.1.  $G^b(\tau_{1(2)})$  is the Green’s function of  $b$ -th bin at  $\tau_{1(2)}$ , and  $\overline{G}(\tau_{1(2)})$  is the

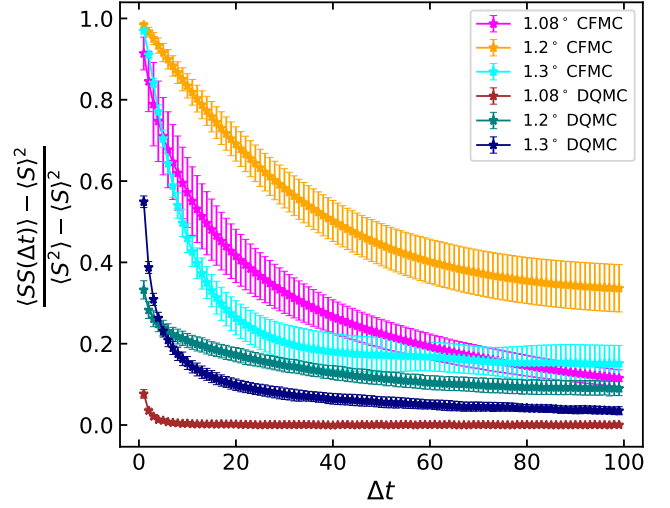


FIG. 8. **Autocorrelation for CFMC and DQMC with  $L = 6$  at different measurement intervals,  $\Delta t$ .** For the simulation at MA, autocorrelation from CFMC at the  $\Delta t = 100$  interval is comparable with that of DQMC at the  $\Delta t = 1$  interval. Thus CFMC is only  $L^2 \times 3/100 = 1.08$  times faster than DQMC in this particular case. However the speedup is much larger for larger  $L$ , since the autocorrelation is not dependent on lattice size. Thus the speedup is 13.5 times for  $L = 15$  simulations at MA. The numbers are similar for  $1.2^\circ$  angle and even more favorable for CFMC at  $1.3^\circ$  angle. In the latter case, the autocorrelation is the same for CFMC at  $\Delta t = 17$  interval as DQMC at  $\Delta t = 1$ , which means another factor of 6 for the speedup even at the smallest lattice .

average of  $G^b(\tau_{1(2)})$  over all bins. Importance sampling of Metropolis-Hastings type is employed and the sampling weight is  $W = \exp(-\chi^2/(2T_1))$  where  $T_1$  is the artificial temperature. According to the general scheme of the stochastic analytical continuation, it decreases starting from 5 by a factor of 0.6 in each step. The final value of  $T_1$  is defined by the average effective action satisfying the relation  $\langle \chi^2 \rangle = \chi_{\min}^2 + 2\sqrt{\chi_{\min}^2}$  [41], and this final value of  $T_1$  is used to obtain the spectra.

### Computation of the free energy

The free energy is difficult to obtain numerically, since exponentially large or small numbers are usually involved. Let us denote the partition function as  $Z = \sum_C W_C P_C$ , where  $W_C$  corresponds to the bosonic part of the action and  $P_C$  corresponds to the fermionic determinant.  $C$  is the configuration of auxiliary fields. Since the kinetic energy is included as  $e^{-\Delta\tau H_0}$  in Eq. 17,  $P_C$  becomes exponentially large as the kinetic energy grows with twisted angle (see Fig. 5). One might think that positive and negative terms in the matrix  $e^{-\Delta\tau H_0}$  form pairs, so that they cancel each other and the magnitude of  $P_C$  does not change a lot with the twisted angle. However, the identity matrix in the relation,  $\text{Tr} \left( e^{\sum_{i,j} c_i^\dagger A_{i,j} c_j} e^{\sum_{i,j} c_i^\dagger B_{i,j} c_j} \right) = \text{Det} (I + e^A e^B)$ , forbids this cancellation.

The free energy  $F$  can be theoretically measured by

$$\begin{aligned}
F &\equiv -\frac{1}{\beta} \ln(Z) \\
&= -\frac{1}{\beta} \ln \left( \sum_C W_C P_C \right) \\
&= -\frac{1}{\beta} \ln \left( \left( \sum_C W_C \right) \frac{\sum_C W_C P_C}{\sum_C W_C} \right) \\
&= -\frac{1}{\beta} \ln \left( \sum_C W_C \right) - \frac{1}{\beta} \ln \left( \frac{\sum_C W_C P_C}{\sum_C W_C} \right),
\end{aligned} \tag{21}$$

which simply means the importance sampling of  $P_C$  over the weight defined by  $W_C$ . However,  $P_C$  is exponentially large in our case, so that direct sampling of a moderate-size system is inaccessible. Recently, an integral algorithm to efficiently sample the exponential observable such as the free energy and entanglement entropy was developed [110]. Dumping the constant number  $-\ln(\sum_C W_C)/\beta$ , we can rewrite  $F$  as

$$F = -\frac{1}{\beta} \int_0^1 dt \frac{\partial \ln(f(t))}{\partial t}, \tag{22}$$

if  $f(1) = (\sum_C W_C P_C)/(\sum_C W_C)$  and  $f(0) = 1$ . Subsequently, we define  $f(t)$  as  $f(t) = \langle e^{tX} \rangle$ , so that  $\langle e^X \rangle = (\sum_C W_C P_C)/(\sum_C W_C)$  and  $X = \ln(P)$ . Substituting it in (22), we get

$$\begin{aligned}
F &= -\frac{1}{\beta} \int_0^1 dt \frac{\langle X e^{tX} \rangle}{\langle e^{tX} \rangle} \\
&= -\frac{1}{\beta} \int_0^1 dt \frac{\sum_C W_C P_C^t \ln(P_C)}{\sum_C W_C P_C^t}.
\end{aligned} \tag{23}$$

Thus, the exponent in observable is avoided and we need only the importance samplings of  $\ln(P_C)$  over the weight of  $W_C P_C^t$ .

### Padé approximants and scaling exponents.

The critical exponents characterize a particular universality class and depend on the dimensionality, symmetry and the relevant degrees of freedom. The transition to the IVC order in TBG falls in the universality class of the chiral XY-Gross-Neveu model. This was considered previously via perturbative renormalisation up to four-loop order in an  $\epsilon$  expansion [70], where  $\epsilon$  is the deviation from the the upper critical spacetime dimension  $D = 4 - \epsilon$  of the model In Ref. [70], a scale dependence is introduced in the fields  $\phi$  and  $\psi$ , as well as for the mass term  $m$ , quartic coupling  $\lambda$ , and Yukawa coupling  $g$  from Eq. (3), and their renormalisation is calculated. Based on this, the inverse correlation-length exponent  $\nu^{-1}$ , the correction-to-scaling exponent  $\omega$ , the fermion and the boson anomalous dimension  $\eta_\psi, \eta_\phi$  are determined and their expression for general fermion flavour number  $N_f$  is provided up to fourth order in  $\epsilon$ . We use these results and apply them to our case of interest, the IVC transition in TBG. To obtain an estimate for the critical exponents for the case of (2+1) dimensions, we

calculate the different Padé approximants

$$P_{[m/n]}(\epsilon) = \frac{a_0 + a_1\epsilon + \dots + a_m\epsilon^m}{1 + b_1\epsilon + \dots + b_n\epsilon^n} \tag{24}$$

for a general fermion flavor number  $N_f$  for the exponents  $\nu^{-1}, \eta_\phi$ . Selecting only those that do not exhibit any singularities or poles, which in our case are  $P_{[2/2]}(\epsilon)$  and  $P_{[3/1]}(\epsilon)$ , we obtain the numerical values for  $N_f = 16$  and  $\epsilon = 1$  and use the hyperscaling relation to determine the order parameter exponent  $\beta$ ,  $\beta = \nu(D - 2 - \eta_\phi)/2$ . We subsequently average over these values and based on those provide the numerical uncertainties. We follow the same procedure to determine the correction-to-scaling exponents  $\omega$ .

### Data availability

The data that support the findings of this study are available from the corresponding author upon reasonable request.

### Code availability

All numerical codes in this paper are available upon reasonable request to the authors.

\* l.classen@fkf.mpg.de

† zymeng@hku.hk

- [1] Y. Cao, V. Fatemi, A. Demir, S. Fang, S. L. Tomarken, J. Y. Luo, J. D. Sanchez-Yamagishi, K. Watanabe, T. Taniguchi, E. Kaxiras, *et al.*, Correlated insulator behaviour at half-filling in magic-angle graphene superlattices, *Nature* **556**, 80 (2018).
- [2] Y. Cao, V. Fatemi, S. Fang, K. Watanabe, T. Taniguchi, E. Kaxiras, and P. Jarillo-Herrero, Unconventional superconductivity in magic-angle graphene superlattices, *Nature* **556**, 43 (2018).
- [3] P. Stepanov, M. Xie, T. Taniguchi, K. Watanabe, X. Lu, A. H. MacDonald, B. A. Bernevig, and D. K. Efetov, Competing zero-field chern insulators in superconducting twisted bilayer graphene, *Phys. Rev. Lett.* **127**, 197701 (2021).
- [4] N. Bultinck, E. Khalaf, S. Liu, S. Chatterjee, A. Vishwanath, and M. P. Zaletel, Ground state and hidden symmetry of magic-angle graphene at even integer filling, *Phys. Rev. X* **10**, 031034 (2020).
- [5] Y. Da Liao, J. Kang, C. N. Brei, X. Y. Xu, H.-Q. Wu, B. M. Andersen, R. M. Fernandes, and Z. Y. Meng, Correlation-induced insulating topological phases at charge neutrality in twisted bilayer graphene, *Phys. Rev. X* **11**, 011014 (2021).
- [6] B. Lian, Z.-D. Song, N. Regnault, D. K. Efetov, A. Yazdani, and B. A. Bernevig, Twisted bilayer graphene. iv. exact insulator ground states and phase diagram, *Phys. Rev. B* **103**, 205414 (2021).
- [7] A. Inbar, J. Birkbeck, J. Xiao, T. Taniguchi, K. Watanabe, B. Yan, Y. Oreg, A. Stern, E. Berg, and S. Ilani, The quantum twisting microscope, *Nature* **614**, 682 (2023).
- [8] N. Parthenios and L. Classen, Twisted bilayer graphene at charge neutrality: Competing orders of su(4) dirac fermions, *Phys. Rev. B* **108**, 235120 (2023).
- [9] G. W. Semenoff, Chiral symmetry breaking in graphene, *Physica Scripta* **T146**, 014016 (2012).
- [10] J. Zinn-Justin, Four-fermion interaction near four dimensions, *Nuclear Physics B* **367**, 105 (1991).

- [11] X. Zhang, G. Pan, Y. Zhang, J. Kang, and Z. Y. Meng, Momentum space quantum monte carlo on twisted bilayer graphene, *Chinese Physics Letters* **38**, 077305 (2021).
- [12] Y. Cao, J. Y. Luo, V. Fatemi, S. Fang, J. D. Sanchez-Yamagishi, K. Watanabe, T. Taniguchi, E. Kaxiras, and P. Jarillo-Herrero, Superlattice-induced insulating states and valley-protected orbits in twisted bilayer graphene, *Phys. Rev. Lett.* **117**, 116804 (2016).
- [13] J. D. Sanchez-Yamagishi, T. Taychatanapat, K. Watanabe, T. Taniguchi, A. Yacoby, and P. Jarillo-Herrero, Quantum hall effect, screening, and layer-polarized insulating states in twisted bilayer graphene, *Phys. Rev. Lett.* **108**, 076601 (2012).
- [14] A. Luican, G. Li, A. Reina, J. Kong, R. R. Nair, K. S. Novoselov, A. K. Geim, and E. Y. Andrei, Single-layer behavior and its breakdown in twisted graphene layers, *Phys. Rev. Lett.* **106**, 126802 (2011).
- [15] H. Schmidt, T. Lüdtkke, P. Barthold, and R. Haug, Temperature dependent measurements on two decoupled graphene monolayers, *Physica E: Low-dimensional Systems and Nanostructures* **42**, 699 (2010), 18th International Conference on Electron Properties of Two-Dimensional Systems.
- [16] S. Shallcross, S. Sharma, E. Kandelaki, and O. A. Pankratov, Electronic structure of turbostratic graphene, *Phys. Rev. B* **81**, 165105 (2010).
- [17] G. Trambly de Laissardière, D. Mayou, and L. Magaud, Localization of dirac electrons in rotated graphene bilayers, *Nano Letters* **10**, 804 (2010).
- [18] R. Bistritzer and A. H. MacDonald, Moiré bands in twisted double-layer graphene, *Proceedings of the National Academy of Sciences* **108**, 12233 (2011).
- [19] J. M. B. Lopes dos Santos, N. M. R. Peres, and A. H. Castro Neto, Continuum model of the twisted graphene bilayer, *Phys. Rev. B* **86**, 155449 (2012).
- [20] A. Datta, M. J. Calderón, A. Camjayi, and E. Bascones, Heavy quasiparticles and cascades without symmetry breaking in twisted bilayer graphene, *Nat. Commun.* **14**, 1 (2023).
- [21] G. Tarnopolsky, A. J. Kruchkov, and A. Vishwanath, Origin of magic angles in twisted bilayer graphene, *Phys. Rev. Lett.* **122**, 106405 (2019).
- [22] B. A. Bernevig, Z.-D. Song, N. Regnault, and B. Lian, Twisted bilayer graphene. iii. interacting hamiltonian and exact symmetries, *Phys. Rev. B* **103**, 205413 (2021).
- [23] Y. Sheffer, R. Queiroz, and A. Stern, Symmetries as the guiding principle for flattening bands of dirac fermions, *Phys. Rev. X* **13**, 021012 (2023).
- [24] X. Lu, P. Stepanov, W. Yang, M. Xie, M. A. Aamir, I. Das, C. Urgell, K. Watanabe, T. Taniguchi, G. Zhang, A. Bachtold, A. H. MacDonald, and D. K. Efetov, Superconductors, orbital magnets and correlated states in magic-angle bilayer graphene, *Nature* **574**, 653 (2019).
- [25] S. Wu, Z. Zhang, K. Watanabe, T. Taniguchi, and E. Y. Andrei, Chern insulators, van hove singularities and topological flat bands in magic-angle twisted bilayer graphene, *Nature Materials* **20**, 488 (2021).
- [26] Y. Cao, D. Chowdhury, D. Rodan-Legrain, O. Rubies-Bigorda, K. Watanabe, T. Taniguchi, T. Senthil, and P. Jarillo-Herrero, Strange metal in magic-angle graphene with near planckian dissipation, *Phys. Rev. Lett.* **124**, 076801 (2020).
- [27] A. Jaoui, I. Das, G. Di Battista, J. Díez-Mérida, X. Lu, K. Watanabe, T. Taniguchi, H. Ishizuka, L. Levitov, and D. K. Efetov, Quantum critical behaviour in magic-angle twisted bilayer graphene, *Nature Physics* **18**, 633 (2022).
- [28] M. Yankowitz, S. Chen, H. Polshyn, Y. Zhang, K. Watanabe, T. Taniguchi, D. Graf, A. F. Young, and C. R. Dean, Tuning superconductivity in twisted bilayer graphene, *Science* **363**, 1059 (2019).
- [29] K. P. Nuckolls, R. L. Lee, M. Oh, D. Wong, T. Soejima, J. P. Hong, D. Călugăru, J. Herzog-Arbeitman, B. A. Bernevig, K. Watanabe, *et al.*, Quantum textures of the many-body wavefunctions in magic-angle graphene, *Nature* **620**, 525 (2023).
- [30] Y.-H. Zhang, H. C. Po, and T. Senthil, Landau level degeneracy in twisted bilayer graphene: Role of symmetry breaking, *Phys. Rev. B* **100**, 125104 (2019).
- [31] D. E. Parker, T. Soejima, J. Hauschild, M. P. Zaletel, and N. Bultinck, Strain-induced quantum phase transitions in magic-angle graphene, *Phys. Rev. Lett.* **127**, 027601 (2021).
- [32] Y. H. Kwan, G. Wagner, T. Soejima, M. P. Zaletel, S. H. Simon, S. A. Parameswaran, and N. Bultinck, Kekulé spiral order at all nonzero integer fillings in twisted bilayer graphene, *Phys. Rev. X* **11**, 041063 (2021).
- [33] G. Wagner, Y. H. Kwan, N. Bultinck, S. H. Simon, and S. A. Parameswaran, Global phase diagram of the normal state of twisted bilayer graphene, *Phys. Rev. Lett.* **128**, 156401 (2022).
- [34] M. Huang, Z. Wu, X. Zhang, X. Feng, Z. Zhou, S. Wang, Y. Chen, C. Cheng, K. Sun, Z. Y. Meng, and N. Wang, Intrinsic nonlinear hall effect and gate-switchable berry curvature sliding in twisted bilayer graphene, *Phys. Rev. Lett.* **131**, 066301 (2023).
- [35] M. Kapfer, B. S. Jessen, M. E. Eisele, M. Fu, D. R. Danielsen, T. P. Darlington, S. L. Moore, N. R. Finney, A. Marchese, V. Hsieh, P. Majchrzak, Z. Jiang, D. Biswas, P. Dudin, J. Avila, K. Watanabe, T. Taniguchi, S. Ulstrup, P. Bøggild, P. J. Schuck, D. N. Basov, J. Hone, and C. R. Dean, Programming twist angle and strain profiles in 2d materials, *Science* **381**, 677 (2023).
- [36] R. Ribeiro-Palau, C. Zhang, K. Watanabe, T. Taniguchi, J. Hone, and C. R. Dean, Twistable electronics with dynamically rotatable heterostructures, *Science* **361**, 690 (2018).
- [37] Y. Yang, J. Li, J. Yin, S. Xu, C. Mullan, T. Taniguchi, K. Watanabe, A. K. Geim, K. S. Novoselov, and A. Mishchenko, In situ manipulation of van der waals heterostructures for twistronics, *Science Advances* **6**, eabd3655 (2020).
- [38] J. S. Hofmann, E. Khalaf, A. Vishwanath, E. Berg, and J. Y. Lee, Fermionic monte carlo study of a realistic model of twisted bilayer graphene, *Phys. Rev. X* **12**, 011061 (2022).
- [39] X. Zhang, G. Pan, B.-B. Chen, H. Li, K. Sun, and Z. Y. Meng, Polynomial sign problem and topological mott insulator in twisted bilayer graphene, *Phys. Rev. B* **107**, L241105 (2023).
- [40] C. Huang, X. Zhang, G. Pan, H. Li, K. Sun, X. Dai, and Z. Y. Meng, Evolution from quantum anomalous hall insulator to heavy-fermion semimetal in magic-angle twisted bilayer graphene, *Phys. Rev. B* **109**, 125404 (2024).
- [41] G. Pan, X. Zhang, H. Li, K. Sun, and Z. Y. Meng, Dynamical properties of collective excitations in twisted bilayer graphene, *Phys. Rev. B* **105**, L121110 (2022).
- [42] X. Zhang, K. Sun, H. Li, G. Pan, and Z. Y. Meng, Superconductivity and bosonic fluid emerging from moiré flat bands, *Phys. Rev. B* **106**, 184517 (2022).
- [43] G. Pan, X. Zhang, H. Lu, H. Li, B.-B. Chen, K. Sun, and Z. Y. Meng, Thermodynamic characteristic for a correlated flat-band system with a quantum anomalous hall ground state, *Phys. Rev. Lett.* **130**, 016401 (2023).
- [44] S. Beyl, F. Goth, and F. F. Assaad, Revisiting the hybrid quantum monte carlo method for hubbard and electron-phonon models, *Phys. Rev. B* **97**, 085144 (2018).
- [45] H. C. Po, L. Zou, A. Vishwanath, and T. Senthil, Origin of mott insulating behavior and superconductivity in twisted bilayer graphene, *Phys. Rev. X* **8**, 031089 (2018).
- [46] N. Bultinck, E. Khalaf, S. Liu, S. Chatterjee, A. Vishwanath,

- and M. P. Zaletel, Ground State and Hidden Symmetry of Magic-Angle Graphene at Even Integer Filling, *Phys. Rev. X* **10**, 031034 (2020).
- [47] B. A. Bernevig, B. Lian, A. Cowsik, F. Xie, N. Regnault, and Z.-D. Song, Twisted bilayer graphene. v. exact analytic many-body excitations in coulomb hamiltonians: Charge gap, goldstone modes, and absence of cooper pairing, *Phys. Rev. B* **103**, 205415 (2021).
- [48] The detailed real space TBG lattice and its Brillouin zone, the analyses of the sign problem and results of various physical observables are given in this Supplemental Material.
- [49] D. J. Gross and A. Neveu, Dynamical symmetry breaking in asymptotically free field theories, *Phys. Rev. D* **10**, 3235 (1974).
- [50] I. F. Herbut, V. Juričić, and B. Roy, Theory of interacting electrons on the honeycomb lattice, *Phys. Rev. B* **79**, 085116 (2009).
- [51] V. Juričić, I. F. Herbut, and G. W. Semenoff, Coulomb interaction at the metal-insulator critical point in graphene, *Phys. Rev. B* **80**, 081405 (2009).
- [52] I. F. Herbut, V. Juričić, and O. Vafek, Relativistic mott criticality in graphene, *Phys. Rev. B* **80**, 075432 (2009).
- [53] B. Roy, V. Juričić, and I. F. Herbut, Emergent lorentz symmetry near fermionic quantum critical points in two and three dimensions, *Journal of High Energy Physics* **2016**, 18 (2016).
- [54] Y. Da Liao, Z. Y. Meng, and X. Y. Xu, Valence bond orders at charge neutrality in a possible two-orbital extended hubbard model for twisted bilayer graphene, *Phys. Rev. Lett.* **123**, 157601 (2019).
- [55] F. F. Assaad and I. F. Herbut, Pinning the order: The nature of quantum criticality in the hubbard model on honeycomb lattice, *Phys. Rev. X* **3**, 031010 (2013).
- [56] Y. Liu, W. Wang, K. Sun, and Z. Y. Meng, Designer monte carlo simulation for the gross-neveu-yukawa transition, *Phys. Rev. B* **101**, 064308 (2020).
- [57] T.-T. Wang and Z. Y. Meng, Quantum monte carlo calculation of critical exponents of the gross-neveu-yukawa on a two-dimensional fermion lattice model, *Phys. Rev. B* **108**, L121112 (2023).
- [58] Y. Da Liao, X. Y. Xu, Z. Y. Meng, and Y. Qi, Dirac fermions with plaquette interactions. iii.  $SU(n)$  phase diagram with gross-neveu criticality and first-order phase transition, *Phys. Rev. B* **106**, 155159 (2022).
- [59] B. Ihrig, L. N. Mihaila, and M. M. Scherer, Critical behavior of dirac fermions from perturbative renormalization, *Phys. Rev. B* **98**, 125109 (2018).
- [60] S. M. Tabatabaei, A.-R. Negari, J. Maciejko, and A. Vaezi, Chiral ising gross-neveu criticality of a single dirac cone: A quantum monte carlo study, *Phys. Rev. Lett.* **128**, 225701 (2022).
- [61] B. Knorr, Ising and gross-neveu model in next-to-leading order, *Phys. Rev. B* **94**, 245102 (2016).
- [62] E. Huffman and S. Chandrasekharan, Fermion bag approach to hamiltonian lattice field theories in continuous time, *Phys. Rev. D* **96**, 114502 (2017).
- [63] Z.-X. Li, Y.-F. Jiang, and H. Yao, Fermion-sign-free majarana-quantum-monte-carlo studies of quantum critical phenomena of dirac fermions in two dimensions, *New Journal of Physics* **17**, 085003 (2015).
- [64] S. Chandrasekharan and A. Li, Quantum critical behavior in three dimensional lattice gross-neveu models, *Phys. Rev. D* **88**, 021701 (2013).
- [65] J. A. Gracey, Critical exponent  $\eta$  at  $o(1/N^3)$  in the chiral xy model using the large  $n$  conformal bootstrap, *Phys. Rev. D* **103**, 065018 (2021).
- [66] L. Iliesiu, F. Kos, D. Poland, S. S. Pufu, and D. Simmons-Duffin, Bootstrapping 3d fermions with global symmetries, *Journal of High Energy Physics* **2018**, 36 (2018).
- [67] Y. Otsuka, K. Seki, S. Sorella, and S. Yunoki, Dirac electrons in the square-lattice hubbard model with a  $d$ -wave pairing field: The chiral heisenberg universality class revisited, *Phys. Rev. B* **102**, 235105 (2020).
- [68] J. GRACEY, Computation of critical exponent  $\eta$  at  $o(1/n^3)$  in the four-fermi model in arbitrary dimensions, *International Journal of Modern Physics A* **09**, 727 (1994).
- [69] J. A. Gracey, Large  $n$  critical exponents for the chiral heisenberg gross-neveu universality class, *Phys. Rev. D* **97**, 105009 (2018).
- [70] N. Zerf, L. N. Mihaila, P. Marquard, I. F. Herbut, and M. M. Scherer, Four-loop critical exponents for the gross-neveu-yukawa models, *Phys. Rev. D* **96**, 096010 (2017).
- [71] T. C. Lang and A. M. Läuchli, Quantum monte carlo simulation of the chiral heisenberg gross-neveu-yukawa phase transition with a single dirac cone, *Phys. Rev. Lett.* **123**, 137602 (2019).
- [72] B. Knorr, Critical chiral heisenberg model with the functional renormalization group, *Phys. Rev. B* **97**, 075129 (2018).
- [73] D. Liu, K. Ishikawa, R. Takehara, K. Miyagawa, M. Tamura, and K. Kanoda, Insulating nature of strongly correlated massless dirac fermions in an organic crystal, *Phys. Rev. Lett.* **116**, 226401 (2016).
- [74] M. Hirata, K. Ishikawa, K. Miyagawa, M. Tamura, C. Berthier, D. Basko, A. Kobayashi, G. Matsuno, and K. Kanoda, Observation of an anisotropic dirac cone reshaping and ferrimagnetic spin polarization in an organic conductor, *Nature Communications* **7**, 12666 (2016).
- [75] M. Hirata, K. Ishikawa, G. Matsuno, A. Kobayashi, K. Miyagawa, M. Tamura, C. Berthier, and K. Kanoda, Anomalous spin correlations and excitonic instability of interacting 2d weyl fermions, *Science* **358**, 1403 (2017).
- [76] I. F. Herbut, Interactions and phase transitions on graphene's honeycomb lattice, *Phys. Rev. Lett.* **97**, 146401 (2006).
- [77] M. Moshe and J. Zinn-Justin, Quantum field theory in the large  $n$  limit: a review, *Physics Reports* **385**, 69 (2003).
- [78] B. Rosenstein, Hoi-Lai Yu, and A. Kovner, Critical exponents of new universality classes, *Physics Letters B* **314**, 381 (1993).
- [79] S. Liu, E. Khalaf, J. Y. Lee, and A. Vishwanath, Nematic topological semimetal and insulator in magic-angle bilayer graphene at charge neutrality, *Phys. Rev. Research* **3**, 013033 (2021).
- [80] M. Ippoliti, R. S. K. Mong, F. F. Assaad, and M. P. Zaletel, Half-filled landau levels: A continuum and sign-free regularization for three-dimensional quantum critical points, *Phys. Rev. B* **98**, 235108 (2018).
- [81] Y. Cao, D. Rodan-Legrain, O. Rubies-Bigorda, J. M. Park, K. Watanabe, T. Taniguchi, and P. Jarillo-Herrero, Tunable correlated states and spin-polarized phases in twisted bilayer-graphene, *Nature* **583**, 215 (2020).
- [82] H. Polshyn, M. Yankowitz, S. Chen, Y. Zhang, K. Watanabe, T. Taniguchi, C. R. Dean, and A. F. Young, Large linear-temperature resistivity in twisted bilayer graphene, *Nature Physics* **15**, 1011 (2019).
- [83] X. Liu, Z. Wang, K. Watanabe, T. Taniguchi, O. Vafek, and J. Li, Tuning electron correlation in magic-angle twisted bilayer graphene using coulomb screening, *Science* **371**, 1261 (2021).
- [84] Y. Xie, B. Lian, B. Jäck, X. Liu, C.-L. Chiu, K. Watanabe, T. Taniguchi, B. A. Bernevig, and A. Yazdani, Spectroscopic signatures of many-body correlations in magic-angle twisted bilayer graphene, *Nature* **572**, 101 (2019).
- [85] Y. Choi, J. Kemmer, Y. Peng, A. Thomson, H. Arora, R. Polski, Y. Zhang, H. Ren, J. Alicea, G. Refael, *et al.*, Electronic

- correlations in twisted bilayer graphene near the magic angle, *Nature physics* **15**, 1174 (2019).
- [86] K. P. Nuckolls, M. Oh, D. Wong, B. Lian, K. Watanabe, T. Taniguchi, B. A. Bernevig, and A. Yazdani, Strongly correlated chern insulators in magic-angle twisted bilayer graphene, *Nature* **588**, 610 (2020).
- [87] Y. Saito, J. Ge, L. Rademaker, K. Watanabe, T. Taniguchi, D. A. Abanin, and A. F. Young, Hofstadter subband ferromagnetism and symmetry-broken chern insulators in twisted bilayer graphene, *Nature Physics* **17**, 478 (2021).
- [88] I. Das, X. Lu, J. Herzog-Arbeitman, Z.-D. Song, K. Watanabe, T. Taniguchi, B. A. Bernevig, and D. K. Efetov, Symmetry-broken chern insulators and rashba-like landau-level crossings in magic-angle bilayer graphene, *Nature Physics* **17**, 710 (2021).
- [89] S. Wu, Z. Zhang, K. Watanabe, T. Taniguchi, and E. Y. Andrei, Chern insulators, van hove singularities and topological flat bands in magic-angle twisted bilayer graphene, *Nature materials* **20**, 488 (2021).
- [90] F. Xie, A. Cowsik, Z.-D. Song, B. Lian, B. A. Bernevig, and N. Regnault, Twisted bilayer graphene. vi. an exact diagonalization study at nonzero integer filling, *Phys. Rev. B* **103**, 205416 (2021).
- [91] P. Potasz, M. Xie, and A. H. MacDonald, Exact diagonalization for magic-angle twisted bilayer graphene, *Phys. Rev. Lett.* **127**, 147203 (2021).
- [92] P. Wilhelm, T. C. Lang, and A. M. Läuchli, Interplay of fractional chern insulator and charge density wave phases in twisted bilayer graphene, *Phys. Rev. B* **103**, 125406 (2021).
- [93] M. Xie and A. H. MacDonald, Nature of the correlated insulator states in twisted bilayer graphene, *Phys. Rev. Lett.* **124**, 097601 (2020).
- [94] Y. Zhang, K. Jiang, Z. Wang, and F. Zhang, Correlated insulating phases of twisted bilayer graphene at commensurate filling fractions: A hartree-fock study, *Phys. Rev. B* **102**, 035136 (2020).
- [95] J. Liu and X. Dai, Theories for the correlated insulating states and quantum anomalous hall effect phenomena in twisted bilayer graphene, *Phys. Rev. B* **103**, 035427 (2021).
- [96] K. Hejazi, X. Chen, and L. Balents, Hybrid wannier chern bands in magic angle twisted bilayer graphene and the quantized anomalous hall effect, *Phys. Rev. Res.* **3**, 013242 (2021).
- [97] F. Xie, J. Kang, B. A. Bernevig, O. Vafek, and N. Regnault, Phase diagram of twisted bilayer graphene at filling factor  $\nu = \pm 3$ , *Phys. Rev. B* **107**, 075156 (2023).
- [98] X. Lin and J. Ni, Symmetry breaking in the double moiré superlattices of relaxed twisted bilayer graphene on hexagonal boron nitride, *Phys. Rev. B* **102**, 035441 (2020).
- [99] Y. H. Kwan, G. Wagner, N. Chakraborty, S. H. Simon, and S. A. Parameswaran, Domain wall competition in the chern insulating regime of twisted bilayer graphene, *Phys. Rev. B* **104**, 115404 (2021).
- [100] A. Datta, M. J. Calderón, A. Camjayi, and E. Bascones, Heavy quasiparticles and cascades without symmetry breaking in twisted bilayer graphene, *arXiv e-prints*, [arXiv:2301.13024](https://arxiv.org/abs/2301.13024) (2023), [arXiv:2301.13024](https://arxiv.org/abs/2301.13024) [cond-mat.str-el].
- [101] J. Kang and O. Vafek, Non-abelian dirac node braiding and near-degeneracy of correlated phases at odd integer filling in magic-angle twisted bilayer graphene, *Phys. Rev. B* **102**, 035161 (2020).
- [102] T. Soejima, D. E. Parker, N. Bultinck, J. Hauschild, and M. P. Zaletel, Efficient simulation of moiré materials using the density matrix renormalization group, *Phys. Rev. B* **102**, 205111 (2020).
- [103] Y. Saito, J. Ge, K. Watanabe, T. Taniguchi, and A. F. Young, Independent superconductors and correlated insulators in twisted bilayer graphene, *Nature Physics* **16**, 926 (2020).
- [104] X. Lu, P. Stepanov, W. Yang, M. Xie, M. A. Aamir, I. Das, C. Urgell, K. Watanabe, T. Taniguchi, G. Zhang, *et al.*, Superconductors, orbital magnets and correlated states in magic-angle bilayer graphene, *Nature* **574**, 653 (2019).
- [105] P. Stepanov, I. Das, X. Lu, A. Fahimniya, K. Watanabe, T. Taniguchi, F. H. Koppens, J. Lischner, L. Levitov, and D. K. Efetov, Untying the insulating and superconducting orders in magic-angle graphene, *Nature* **583**, 375 (2020).
- [106] G. Rai, L. Crippa, D. Călugăru, H. Hu, F. Paoletti, L. De' Medici, A. Georges, B. A. Bernevig, R. Valentí, G. Sangiovanni, and T. Wehling, Dynamical Correlations and Order in Magic-Angle Twisted Bilayer Graphene, *Phys. Rev. X* **14**, 031045 (2024).
- [107] A. W. Sandvik, Stochastic method for analytic continuation of quantum monte carlo data, *Phys. Rev. B* **57**, 10287 (1998).
- [108] K. S. D. Beach, Identifying the maximum entropy method as a special limit of stochastic analytic continuation, *arXiv e-prints*, [cond-mat/0403055](https://arxiv.org/abs/cond-mat/0403055) (2004), [arXiv:cond-mat/0403055](https://arxiv.org/abs/cond-mat/0403055) [cond-mat.str-el].
- [109] This is because to compute the free energy, one need to evaluate  $\langle e^{-F} \rangle$  instead of the  $F$  in the path-integral QMC, and that is an exponentially small number, hence the name of exponential observable. Incremental method is one way to carry out its calculation gradually.
- [110] X. Zhang, G. Pan, B.-B. Chen, K. Sun, and Z. Y. Meng, Integral algorithm of exponential observables for interacting fermions in quantum monte carlo simulations, *Phys. Rev. B* **109**, 205147 (2024).
- [111] Y.-D. Liao, X.-Y. Xu, Z.-Y. Meng, and J. Kang, Correlated insulating phases in the twisted bilayer graphene, *Chinese Physics B* **30**, 017305 (2021).
- [112] S. M. Chester, W. Landry, J. Liu, D. Poland, D. Simmons-Duffin, N. Su, and A. Vichi, Carving out ope space and precise o(2) model critical exponents, *Journal of High Energy Physics* **2020**, 142 (2020).
- [113] M. Campostrini, M. Hasenbusch, A. Pelissetto, P. Rossi, and E. Vicari, Critical behavior of the three-dimensional XY universality class, *Phys. Rev. B* **63**, 214503 (2001).
- [114] H.-K. Tang, J. N. Leaw, J. N. B. Rodrigues, I. F. Herbut, P. Sengupta, F. F. Assaad, and S. Adam, The role of electron-electron interactions in two-dimensional Dirac fermions, *Science* **361**, 570 (2018), <http://science.sciencemag.org/content/361/6402/570.full.pdf>.
- [115] M. Hohenadler, F. Parisen Toldin, I. F. Herbut, and F. F. Assaad, Phase diagram of the kane-mele-coulomb model, *Phys. Rev. B* **90**, 085146 (2014).
- [116] P. Buividovich, D. Smith, M. Ulybyshev, and L. von Smekal, Hybrid monte carlo study of competing order in the extended fermionic hubbard model on the hexagonal lattice, *Phys. Rev. B* **98**, 235129 (2018).
- [117] Z. Wang, M. P. Zaletel, R. S. K. Mong, and F. F. Assaad, Phases of the  $(2+1)$  dimensional so(5) nonlinear sigma model with topological term, *Phys. Rev. Lett.* **126**, 045701 (2021).
- [118] J. S. Hofmann, F. Goth, W. Zhu, Y.-C. He, and E. Huffman, Quantum Monte Carlo simulation of the 3D Ising transition on the fuzzy sphere, *SciPost Phys. Core* **7**, 028 (2024).
- [119] B.-B. Chen, X. Zhang, Y. Wang, K. Sun, and Z. Y. Meng, Phases of  $(2+1)$ D so(5) nonlinear sigma model with a topological term on a sphere: Multicritical point and disorder phase, *Phys. Rev. Lett.* **132**, 246503 (2024).
- [120] J. Cai, E. Anderson, C. Wang, X. Zhang, X. Liu, W. Holtzmann,

- Y. Zhang, F. Fan, T. Taniguchi, K. Watanabe, Y. Ran, T. Cao, L. Fu, D. Xiao, W. Yao, and X. Xu, Signatures of fractional quantum anomalous hall states in twisted mote2, *Nature* **622**, 63 (2023).
- [121] H. Park, J. Cai, E. Anderson, Y. Zhang, J. Zhu, X. Liu, C. Wang, W. Holtzmann, C. Hu, Z. Liu, T. Taniguchi, K. Watanabe, J.-H. Chu, T. Cao, L. Fu, W. Yao, C.-Z. Chang, D. Cobden, D. Xiao, and X. Xu, Observation of fractionally quantized anomalous hall effect, *Nature* **622**, 74 (2023).
- [122] Z. Lu, T. Han, Y. Yao, A. P. Reddy, J. Yang, J. Seo, K. Watanabe, T. Taniguchi, L. Fu, and L. Ju, Fractional quantum anomalous hall effect in multilayer graphene, *Nature* **626**, 759 (2024).
- [123] Z. Lu, T. Han, Y. Yao, J. Yang, J. Seo, L. Shi, S. Ye, K. Watanabe, T. Taniguchi, and L. Ju, Extended Quantum Anomalous Hall States in Graphene/hBN Moiré Superlattices, *arXiv e-prints*, arXiv:2408.10203 (2024), arXiv:2408.10203 [cond-mat.mes-hall].
- [124] Y.-Y. He, X. Y. Xu, K. Sun, F. F. Assaad, Z. Y. Meng, and Z.-Y. Lu, Dynamical generation of topological masses in dirac fermions, *Phys. Rev. B* **97**, 081110 (2018).
- [125] C. Bonati, A. Franchi, A. Pelissetto, and E. Vicari, Chiral critical behavior of 3d lattice fermionic models with quartic interactions, *Phys. Rev. D* **107**, 034507 (2023).
- [126] R. S. Erramilli, L. V. Iliesiu, P. Kravchuk, A. Liu, D. Poland, and D. Simmons-Duffin, The gross-neveu-yukawa archipelago, *Journal of High Energy Physics* **2023**, 36 (2023).
- [127] I. F. Herbut, Interactions and phase transitions on graphene's honeycomb lattice, *Phys. Rev. Lett.* **97**, 146401 (2006).
- [128] J. A. Gracey, T. Luthe, and Y. Schröder, Four loop renormalization of the gross-neveu model, *Phys. Rev. D* **94**, 125028 (2016).
- [129] L. N. Mihaila, N. Zerf, B. Ihrig, I. F. Herbut, and M. M. Scherer, Gross-neveu-yukawa model at three loops and ising critical behavior of dirac systems, *Phys. Rev. B* **96**, 165133 (2017).
- [130] R. Blankenbecler, D. J. Scalapino, and R. L. Sugar, Monte carlo calculations of coupled boson-fermion systems. i, *Phys. Rev. D* **24**, 2278 (1981).
- [131] S. R. White, D. J. Scalapino, R. L. Sugar, E. Y. Loh, J. E. Gubernatis, and R. T. Scalettar, Numerical study of the two-dimensional hubbard model, *Phys. Rev. B* **40**, 506 (1989).
- [132] F. Assaad and H. Evertz, World-line and determinantal quantum monte carlo methods for spins, phonons and electrons, in *Computational Many-Particle Physics*, edited by H. Fehske, R. Schneider, and A. Weiße (Springer Berlin Heidelberg, Berlin, Heidelberg, 2008) pp. 277–356.
- [133] M. Berx, F. Goth, J. S. Hofmann, and F. F. Assaad, The alf (algorithms for lattice fermions) project release 1.0. documentation for the auxiliary field quantum monte carlo code, *SciPost Physics* **3**, 013 (2017).
- [134] J. E. Hirsch, Discrete hubbard-stratonovich transformation for fermion lattice models, *Phys. Rev. B* **28**, 4059 (1983).
- [135] X. Zhang, G. Pan, X. Y. Xu, and Z. Y. Meng, Fermion sign bounds theory in quantum monte carlo simulation, *Phys. Rev. B* **106**, 035121 (2022).
- [136] P. Buividovich, D. Smith, M. Ulybyshev, and L. von Smekal, Numerical evidence of conformal phase transition in graphene with long-range interactions, *Phys. Rev. B* **99**, 205434 (2019).
- [137] B.-B. Chen, X. Zhang, and Z. Y. Meng, Emergent conformal symmetry at the multicritical point of  $(2 + 1)D$  so(5) model with wess-zumino-witten term on a sphere, *Phys. Rev. B* **110**, 125153 (2024).
- [138] J. Lee and S. Sachdev, Wess-zumino-witten terms in graphene landau levels, *Phys. Rev. Lett.* **114**, 226801 (2015).
- [139] M. Ulybyshev and F. Assaad, Mitigating spikes in fermion monte carlo methods by reshuffling measurements, *Phys. Rev. E* **106**, 025318 (2022).
- [140] B. A. Bernevig, B. Lian, A. Cowsik, F. Xie, N. Regnault, and Z.-D. Song, Twisted bilayer graphene. V. Exact analytic many-body excitations in Coulomb Hamiltonians: Charge gap, Goldstone modes, and absence of Cooper pairing, *Phys. Rev. B* **103**, 205415 (2021).

## Acknowledgments

We thank Michael Scherer for valuable input on the critical exponents from  $4 - \epsilon$  expansion and acknowledge discussions with Lukas Janssen on similar topic. C.H. and Z.Y.M. acknowledge the support from the Research Grants Council (RGC) of Hong Kong Special Administrative Region (SAR) of China (Project Nos. 17301721, AoE/P701/20, 17309822, C7037-22GF, 17302223, 17301924), the ANR/RGC Joint Research Scheme sponsored by RGC of Hong Kong and French National Research Agency (Project No. A HKU703/22) and the HKU Seed Funding for Strategic Interdisciplinary Research. L.C. was funded by the European Union (ERC-2023-STG, Project 101115758 - QuantEmerge). Views and opinions expressed are, however, those of the author only and do not necessarily reflect those of the European Union or the European Research Council Executive Agency. Neither the European Union nor the granting authority can be held responsible for them. M.U. and F.F.A. thank the DFG for financial support under the projects AS120/19-1, Project number 530989922. F.F.A acknowledges financial support from the DFG through the Würzburg-Dresden Cluster of Excellence on Complexity and Topology in Quantum Matter - *ct.qmat* (EXC 2147, Project No. 390858490) as well as the SFB 1170 on Topological and Correlated Electronics at Surfaces and Interfaces (Project No. 258499086). We thank HPC2021 system under the Information Technology Services and the Blackbody HPC system at the Department of Physics, University of Hong Kong, as well as the Beijing PARATERA Tech CO.,Ltd. (URL: <https://cloud.paratera.com>) for providing HPC resources that have contributed to the research results reported within this paper.

## Supplemental Material for "Angle-Tuned Gross-Neveu Quantum Criticality in Twisted Bilayer Graphene: a Quantum Monte Carlo study"

### COMPARISON OF THE CRITICAL EXPONENTS

Here we show the data collapse of the IVC order parameter with the (2+1)D XY exponents. Compared with the data in Fig. 3 in the main text, it is clear that the (2+1)D XY exponents, without the involvement of the Dirac fermion of the GN chiral XY exponents, cannot faithfully describe the data and the transitions, as shown in Fig. 9 (b).

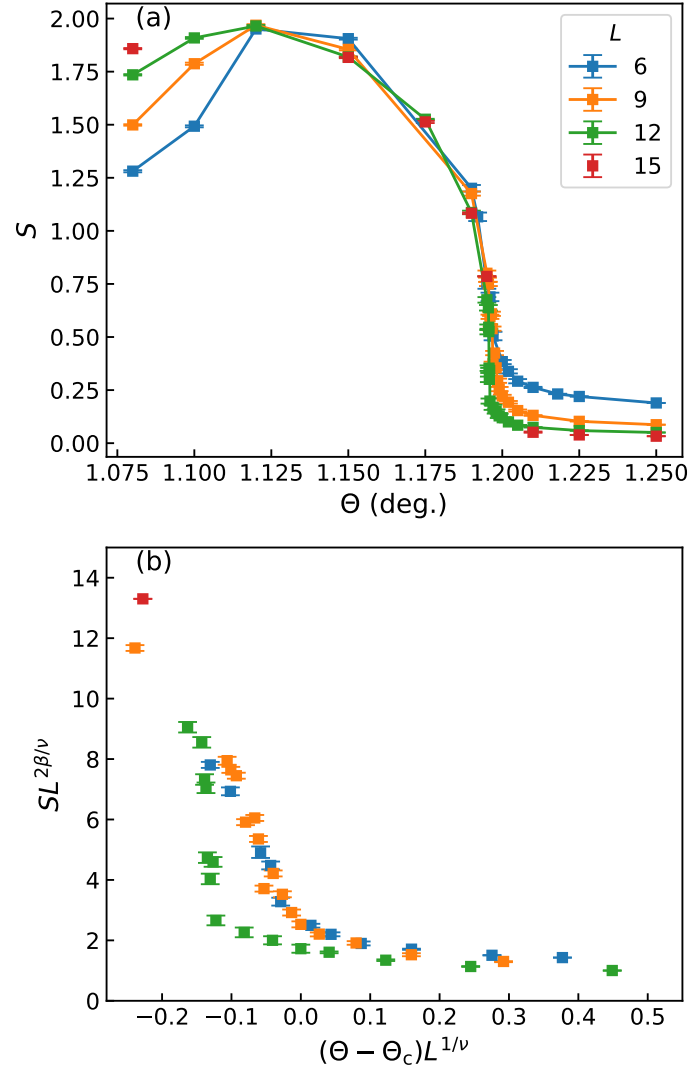


FIG. 9. **The (2+1)D XY analysis from the IVC order parameter.** (a) The structure factor  $S$  of IVC order parameter with the  $L = 6, 9, 12,$  and  $15$  as a function of  $\Theta$ , and  $\beta \propto L$ . From MA to  $1.4^\circ$ , the IVC order continuously vanishes (although there are strong finite size effect close to MA and the peaks of IVC order might actually stand at  $1.08^\circ < \Theta < 1.2^\circ$ ) as the systems evolve from IVC insulator to Dirac semimetal. (b) With the estimated (2+1)D XY GN-QCP exponents,  $\beta = 0.35$  and  $\nu = 0.67$ , and the  $\Theta_c = 1.20(1)^\circ$ , the data collapse indicates the transition is probably not the (2+1)D XY symmetry-breaking order at  $\Theta < \Theta_c$  and the establishment of the Dirac fermions at  $\Theta > \Theta_c$ .



### COMPARISON WITH EXACT GROUNDSTATE OF THE INTERACTING HAMILTONIAN

Following Ref. [140], we calculate the charge  $\pm 1$  excitations when the kinetic energy is omitted. Based on the symmetry arguments therein, for this case the ground state at  $\nu = 0$ , which is the case we consider in this manuscript is exact and given in terms of a product state,  $|\Psi\rangle = \prod_{\eta,s,i} c_{\eta,s,i}^\dagger |0\rangle$ , which satisfies  $\delta\rho_{\mathbf{Q}}|\Psi\rangle = 0$ . Therefore,

$$\begin{aligned} [H_1, c_{s,\eta,\mathbf{k},m}^\dagger] |\Psi\rangle &= H_1 c_{s,\eta,\mathbf{k},m}^\dagger |\Psi\rangle \\ &= \frac{1}{2\Omega} \sum_n R_{mn}^{s,\eta}(\mathbf{k}) c_{s,\eta,\mathbf{k},n}^\dagger |\Psi\rangle, \end{aligned} \quad (25)$$

Notably, in this limit the ground state forms a degenerate U(4) manifold. We can obtain the charge gaps by diagonalizing

$$R_{mn}^{s,\eta}(\mathbf{k}) = \sum_{\mathbf{Q},m'} V(\mathbf{Q}) \lambda_{m,m'}^{s,\eta,*}(\mathbf{k}, \mathbf{Q}) \lambda_{n,m'}^{s,\eta}(\mathbf{k}, \mathbf{Q}). \quad (26)$$

The charge gaps from this expression are used to compare with those from our CFMC simulations. We find that the gaps obtained from both methods are almost identical near the MA ( $\Theta = 1.08^\circ$ , where the bandwidth of the flat bands becomes minimal and the Coulomb repulsion dominates). The inclusion of the kinetic energy splits the U(4) degeneracy and picks out the K-IVC state as has also been described in Refs. [38, 46]. Further increasing the angle, we see a considerable deviation and the emergence of Dirac cones at  $K_{1,2}$  due to the kinetic energy having a sizable contribution.

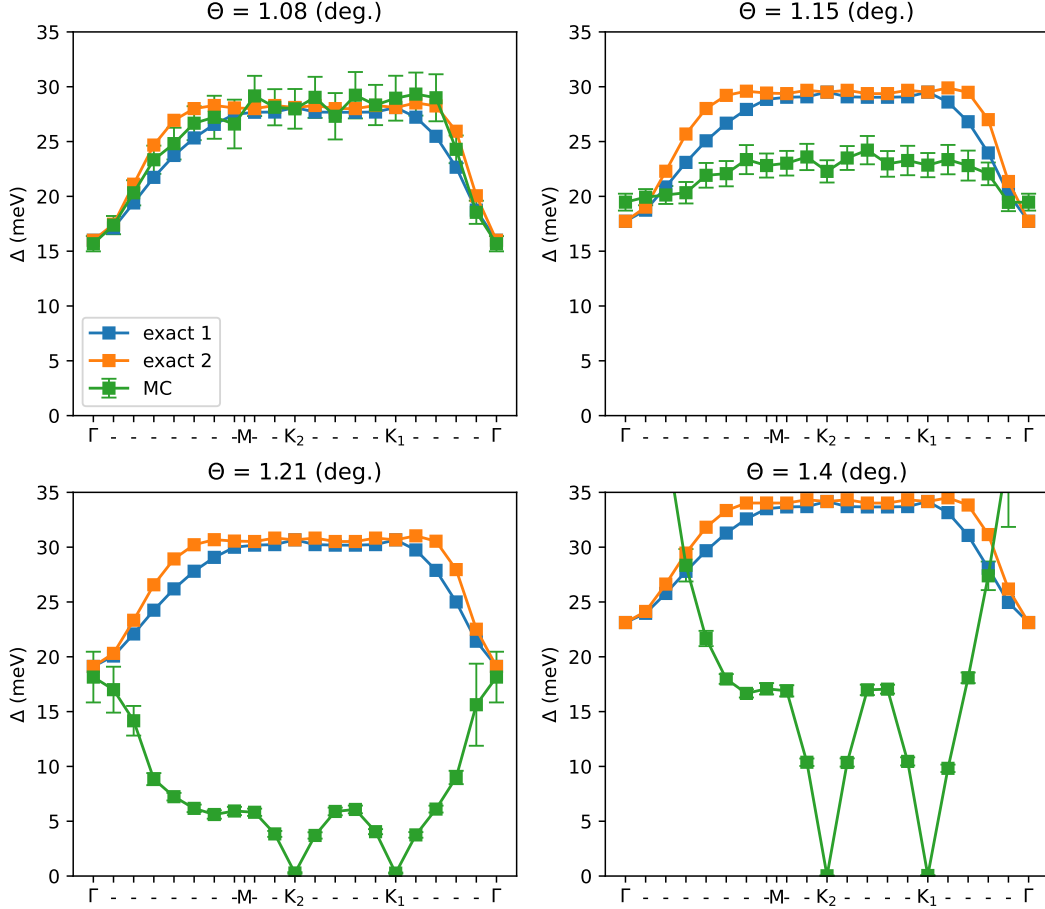


FIG. 10. Comparison between the gaps obtained from Eq. 26 and the CFMC. This indicates that the non-trivial inclusion of the kinetic energy leads to the gaps closing and the emergence of Dirac cones. Note that the gaps obtained from two methods are comparable at the MA.